

1 **Effect of perturbations by shoal margin collapses on the**
2 **morphodynamics of a sandy estuary**

3 **W. M. van Dijk¹, M. R. Hiatt^{1,2}, J. J. van der Werf^{3,4}, and M. G. Kleinans¹**

4 ¹Department of Physical Geography, Faculty of Geosciences, Utrecht University, Utrecht, The Netherlands

5 ²Department of Oceanography and Coastal Sciences, College of the Coast and Environment, Louisiana State University,
6 Baton Rouge, Louisiana, United States

7 ³Department of Marine and Coastal Systems, Deltares, Delft, The Netherlands

8 ⁴Department of Water Engineering and Management, Faculty of Engineering Technology, University of Twente, Enschede,
9 The Netherlands

10 **Key Points:**

- 11 • Shoal margin collapses perturb the channel-shoal network of sandy estuaries.
12 • Disturbances cause long-term morphological changes.
13 • Disturbances amplify asymmetry and instability at channel junctions.

Corresponding author: Wout van Dijk, W.M.vanDijk@uu.nl

Abstract

Shoal margin collapses of several Mm^3 have occurred in the Western Scheldt estuary, the Netherlands, on average five times a year over the last decades. While these collapses involve significant volumes of material, their effect on the channel-shoal morphology is unknown. We hypothesise that collapses dynamicise the channel-shoal interactions, which could impact the ecological functioning, flood safety and navigation in the estuary. The objective is to investigate how locations, probability, type and volume of shoal margin collapse affect the channel-shoal dynamics. We implemented an empirically-validated parameterization for shoal margin collapses and tested its effect on simulated estuary morphological development in a Delft3D schematization of the Western Scheldt. Three sets of scenarios were analyzed for near-field and far-field effects on flow pattern and channel-shoal morphology: 1) an observed shoal margin collapse of 2014, 2) initial large collapses on 10 locations, and 3) continuous collapses predicted by our novel probabilistic model over a time span of decades. Results show that single shoal margin collapses only affect the local dynamics in the longitudinal flow direction and dampen out within a year for typical volumes, whereas larger disturbances that reach the seaward or landward sill at tidal channel junctions grow. The redistribution of the collapsed sediment is determined by the direction of the strongest tidally-averaged flow. We conclude that adding the process of shoal margin collapses increases the channel-shoal interactions, and that in intensively dredged estuaries shoal margins oversteepen, amplifying the number of collapses, but because of dredging the natural morphological response is interrupted.

Keywords: estuary; shoal margin collapse; channel-shoal morphodynamics; tidal bars; Western Scheldt

1 Introduction

The process of channel bank failure and collapses of shoal margins has been recognized in estuaries and rivers around the world [Coleman, 1969; Laury, 1971; Silvis and De Groot, 1995; Torrey, 1995; Dunbar et al., 1999; Van den Berg et al., 2002; Beinssen et al., 2014] but their effect on long-term morphological development remains unknown. The implementation of channel bank failure in numerical morphodynamic models has been studied more recently [Kleinhans, 2010; Nicholas, 2013a; Schuurman et al., 2013] but mainly focussed on outer cut bank erosion in rivers. Though, channel banks can also collapse at the inner bank of rivers [Nieuwboer, 2012]. While collapses of shoal margins are more often observed at the inner side of a bend in estuaries [Wilderom, 1972; Mastbergen and Van den Berg, 2003; Van Dijk et al., 2018a]. Because of the relative large volume of up to several million m^3 that is involved, the associated displaced sediment in the channel perturbs the sediment transport, affecting channel geometry, e.g., the width-depth ratio, and channel dynamics. We hypothesize that such morphological perturbations within the system may amplify the sediment transport in estuaries as much as extreme events imposed in the boundary conditions, indirectly affecting the morphological changes. This is important because morphological models of estuaries invariably evolve towards bar-scale equilibrium [Van der Wegen and Roelvink, 2012; Dam, 2017]. This means that the channel-shoal dynamics are presently underpredicted because of internal dynamics and disturbances, such as collapses, are not captured in the model.

Effects of disturbances and perturbations on morphology in rivers and estuaries have been studied in the past century. The damping and lag associated with environmental disturbances propagating through a system are determined by the magnitude and timescale of the event [Paola et al., 1992; Whipple and Tucker, 1999]. The nonlinear dynamics of sediment transport limits the potential to record and pass on physical environmental disturbances and perturbations [Jerolmack and Paola, 2010]. Such disturbances for fluvial systems have been subdivided into four categories [Schuurman et al., 2016a]: (i) external temporal perturbation of the upstream inflow, (ii) external spatial perturbation, e.g. along

65 the outer channel banks, (iii) external perturbation at the downstream boundary, and (iv)
66 internal perturbations within the reach. Shoal margin collapses fall within the fourth group
67 of disturbances as sediment is eroded from the shoal within the estuary system. Bank ero-
68 sion results in local widening of the system [Khan and Islam, 2003; Ashworth and Lewin,
69 2012], and outer bank erosion is linked to bar (shoal) dynamics, as the eroded sediment is
70 a source for bars [Xu, 1997; Ahktar et al., 2011; Van de Lageweg et al., 2014]. This study
71 focuses on the perturbing effects of shoal margin collapses in estuaries, where flow is bi-
72 directional due to tidal forcing. In tidal systems flow direction depends on the flood ebb
73 asymmetry within the estuary as well as seasonal influences, particularly in the upper es-
74 tuary due to higher fluvial flows during large riverine flooding or lower fluvial flows over
75 drier periods.

76 To study the role of disturbance on the morphology of estuaries, the most control is
77 offered by numerical models. Numerical morphodynamic models are useful tools, but in-
78 teraction with bank erosion processes introduces complications [Canestrelli et al., 2016].
79 The forecasting of these interactions is not commonly addressed due to the complexity of
80 coupling short term geotechnical processes with long-term morphological development.
81 The use of curvilinear grids leads to some complications when modeling abrupt changes
82 such as bank erosion or collapses [Kleinhans, 2010], which might be overcome using un-
83 structured grids and cut-cell techniques [Olsen, 2003; Canestrelli et al., 2016]. Despite
84 successes in including bank erosion processes [Darby et al., 2002; Simon and Collinson,
85 2002; Kleinhans, 2010], erodible floodplains mainly experience outer bank erosion pro-
86 cesses [Nicholas, 2013a,b; Schuurman et al., 2013, 2016b], while collapses due to flow
87 slides, such as liquefaction or breaching processes, that also occur on the inner side of
88 bends in estuaries are under-represented. However, their potential effects are considerable:
89 a single shoal margin collapse can displace several Mm^3 within hours as observed for
90 the collapse in 2014 in the Western Scheldt [Van Schaick, 2015; Mastbergen et al., 2016;
91 Van den Berg et al., 2017; Van Dijk et al., 2018a]. The timing of the collapse determines
92 the respond to the event, which is likely to be different around slack water than at peak
93 flow.

94 Shoal margin collapses through flow slides often occur suddenly, which makes them
95 difficult to predict in current numerical morphodynamic models, such as Delft3D. Shoal
96 margin collapses occur at sufficiently high and steep slopes, but there is a difference in
97 the sediment properties between these two types of flow slides, liquefaction and breach-
98 ing [Van den Ham et al., 2014]. Liquefaction requires loosely packed, non-lithified, and
99 water-saturated sand or silt, whereas breaching requires the presence of a sufficiently large
100 body of densely packed fine sand or silt [Van den Ham et al., 2014]. These processes have
101 been represented by various models but not implemented in a numerical morphodynamic
102 model. Van den Ham et al. [2014] argued that these theoretical liquefaction and breach-
103 ing models quantify the relative influences of channel geometry and soil parameters but
104 the reliability of the estimated probability remains limited. Therefore, Van den Ham et al.
105 [2014] proposed a semi-empirical model that predicts the probability of shoal margin col-
106 lapses on profiles, which was modified and extended for application on spatial bathymetry
107 data by Van Dijk et al. [2018a]. This predictor includes an empirical factor based on the
108 frequency of historical flow slides in the Eastern Scheldt and Western Scheldt estuaries
109 [Wilderom, 1979; Van Dijk et al., 2018a], which is applied in this study instead of the full
110 process-based modeling of flow slides.

111 Our objective is to increase understanding of the interactions between shoal margin
112 collapses and the channel dynamics of a sandy estuary, the relevant timescales and the
113 large-scale morphological effects. The posed research questions are: (i) what are the local
114 (near-field) effects of individual shoal margin collapses, such as the observed 2014 shoal
115 margin collapse? (ii) How do multiple shoal margin collapses affect the channel dynam-
116 ics of the estuary (far-field effect)? Our method was to first use the numerical morphody-
117 namic model Delft3D, to implement an effective parametrization for the process of shoal

margin collapses in a calibrated model. We then study how disturbances, such as multiple collapses, propagate and change the channel-shoal interactions of the Western Scheldt, a sandy estuary. Furthermore, we test the role of grain-size and shoal margin collapse size and location of the associated collapsed deposit on the sediment transport and morphological development. In this paper, we first give a detailed description of the study area, the method for implementation of the shoal margin collapses in Delft3D, and the tested scenarios. Then, we present the near-field and far-field effects of shoal margin collapses on the short-term as well as the long-term morphodynamics of the Western Scheldt. Finally, we discuss the model performance and the implications of persistent perturbations on a sandy estuary.

2 Study Area

This study focuses on shoal margin collapses in the Western Scheldt. The Western Scheldt is located in the southwestern part of the Netherlands ($51^{\circ}41'51''\text{N}$, $5^{\circ}40'35''\text{E}$) and is the seaward section (60 km) of the 200 km tide-dominated Scheldt estuary. The Scheldt is a well-studied and monitored estuary [e.g., Wang *et al.*, 1999; Winterwerp *et al.*, 2000; Bolle *et al.*, 2010; Van der Wegen and Roelvink, 2012] that provides access to various harbors, of which the port of Antwerp (Belgium) is the largest. The Western Scheldt is characterized by a convergent geometry, and has a well-developed system of channels and shoals (Figure 1a).

Channel bank failures have been recorded systematically in the Western Scheldt for the past 200 years [Wilderom, 1961, 1979]. Over the years, bank protection measures have been implemented to protect the channel banks and dikes of the Western Scheldt against new failures and collapses. However, these measures did not fully prevent the occurrence of shoal margin collapses [Wilderom, 1972]. A recent study identifies 300 shoal margin collapses between 1959-2015 [Figure 1a, Van Dijk *et al.*, 2018a], ranging from very small collapsed volumes of $20,000 \text{ m}^3$ up to volumes of $3,000,000 \text{ m}^3$. The majority of the collapses are found at unprotected areas. Relatively fine sediment is found in the estuary, which affects the occurrence of shoal margin collapses [Van den Ham *et al.*, 2014]. In general, the D_{50} of the channel bed varies between about $200 \mu\text{m}$ and $300 \mu\text{m}$, whereas at the higher elevation areas of the shoals the sediment size is generally finer than $200 \mu\text{m}$ [Cancino and Neves, 1999; De Vriend *et al.*, 2011]. Additionally, a significant percentage up to 25% of mud can be found in the intertidal areas but increases toward the flanks [Braat *et al.*, 2017; Van de Lageweg *et al.*, 2018].

The natural development of the morphology as well as the effect of perturbations is the result of interactions between water flow, sediment transport and bed elevation. An important factor causing bi-directional flow and mean sediment transport is the tidal forcing in the Western Scheldt [Wang *et al.*, 1999]. From the mouth of the estuary to the Dutch/Belgian border, the tidal range increases from 3.5 m to 5 m [Jeuken, 2000]. The tidal prism at the mouth is about two billion m^3 [Wang *et al.*, 1999], whereas the yearly-averaged river discharge of the Scheldt into the Western Scheldt is a negligible $120 \text{ m}^3/\text{s}$ [Cancino and Neves, 1999; De Vriend *et al.*, 2011] but peak discharge are observed up to $600 \text{ m}^3/\text{s}$ [Baeyens *et al.*, 1997]. The Western Scheldt has several recirculation zones of sediment through the ebb and flood channels, which enclose the inter-tidal flats [Figure 1b, Wang *et al.*, 1995; Winterwerp *et al.*, 2000]. The tidal flow is asymmetric, i.e., slower but longer ebb flows compared to flood flows (Figure 1c–d). The difference between the maximum flow velocity for ebb and flood illustrated that the flood is generally stronger (Figure 1e) even in the ebb dominated channels as illustrated by the tidally-averaged flow (Figure 1b).

166 3 Model description and methods

167 3.1 Model setup and boundary conditions

168 In this study, we used two Delft3D schematizations that are both based on the NeVla-
 169 Delft3D model of the Scheldt estuary, which includes the upstream Flemish branches of
 170 the estuary, the Western Scheldt and part of the North Sea. The NeVla model is a state-
 171 of-the-art numerical model that has been optimized for hydrodynamics [*Maximova et al.*,
 172 2009a,b,c; *Vroom et al.*, 2015] and morphology [*Grasmeijer et al.*, 2013; *Schrijvershof and*
 173 *Vroom*, 2016]. To study the effect of shoal margin collapses we focused on the Western
 174 Scheldt part of the NeVla model. Therefore, two nested models were produced from the
 175 NeVla-Delft3D model for reducing the computational time. The first nested model bound-
 176 aries (model 1) were located around the tidal flat of Walsoorden (see boundaries in Fig-
 177 ure 1a), which was used to study the morphodynamic response of the 2014 shoal mar-
 178 gin collapses and the sensitivity to collapse sizes, grain-size of the collapsed material,
 179 and location of the collapsed deposits [see also *Van Schaick*, 2015]. *Van Schaick* [2015]
 180 validated the water level and discharge from the nested model with the NeVla-Delft3D
 181 model as well as the response of the 2014 collapse, and concluded that the errors were
 182 small enough to be neglected for the area of interest. The second nested model boundaries
 183 (model 2) include the Western Scheldt from the mouth at Vlissingen to the Belgian border
 184 (see seaward boundaries in Figure 1a), which was used for testing the effect of shoal mar-
 185 gin collapse locations as well as the effect of multiple shoal margin collapses in the West-
 186 ern Scheldt over time. The downstream boundary was chosen at the smallest but deepest
 187 part of the Western Scheldt to limit boundary effects. A single spring-neap-spring cycle
 188 shows that the tidally-averaged flow of this model (Supplementary Figure 4b) is compa-
 189 rable with the outcome of the full NeVla-Delft3D model (Figure 1b), except for a small
 190 variation at the seaward end.

191 The nested model consists of a curvilinear grid with various grid sizes. The bound-
 192 ary conditions include a water level fluctuation due to tides at the seaward boundary and
 193 a current at the landward boundary. Sediment fraction was uniform, with a median grain-
 194 size of 200 μm . For simplification of the boundary conditions, boundary conditions were
 195 selected from a single spring-neap-spring tide cycle of January 2013 (about 14 days) and
 196 repeated for a 2 year period. Furthermore, we excluded the wind direction and magnitude
 197 from the NeVla model to reduce computational time as the effect of wind is negligible
 198 within the Western Scheldt. The roughness field in the model is defined in Manning n
 199 and is variable over the model domain [*Maximova et al.*, 2009a,b,c; *Vroom et al.*, 2015],
 200 which was $0.022 \text{ s}\cdot\text{m}^{-1/3}$ for the eastern part, $0.027 \text{ s}\cdot\text{m}^{-1/3}$ for the western part and 0.028
 201 $\text{ s}\cdot\text{m}^{-1/3}$ for the Verdrongen Land van Saeftinghe. The bed consisted of erodible and non-
 202 erodible layers [*Gruijters et al.*, 2004], the non-erodible layers are formed due to former
 203 deposits that are hardly erodible [*Dam*, 2013], and therefore the sediment thickness varies
 204 within the Western Scheldt model (Supplementary Figure 1). Because sediment transport
 205 was calculated by *Van Rijn* [2007a,b], the bedload and suspended load transport could be
 206 separated.

207 3.2 Transverse bed slope and morphological factor

208 The Delft3D model (version FLOW 6.01.07.3574, 2 April 2014) has been applied in
 209 many scientific projects to compute hydrodynamics, sediment transport, and morphologi-
 210 cal changes [*Roelvink*, 2006; *Deltares*, 2009; *Crosato and Saleh*, 2011; *Van der Wegen and*
 211 *Roelvink*, 2012; *Schuurman et al.*, 2013, 2016a; *Van Dijk et al.*, 2014]. In this study, we
 212 applied a 2D depth-averaged flow field, which meant that the effect of helical flow driven
 213 by flow curvature on bed shear-stress direction were parametrized [*Schuurman et al.*, 2013;
 214 *Baar et al.*, 2018b,a]. The parametrization affected the transverse bed slopes at the shoal
 215 margins, which influenced the moment that shoal margin collapses were predicted. There-
 216 fore, we performed a sensitivity analysis to determine how the sediment transport direc-

tion affects the slopes for α_{bn} between 1.5 and 100 [see Supplementary Text S1, *Bagnold*, 1966; *Ikeda*, 1982a,b; *van Rijn*, 1993]. To reduce computational time, Delft3D includes a morphological acceleration factor M . We performed a sensitivity analysis to determine what effect M has on the morphology of the estuary (see Supplementary Text S1). Based on these analyses we set α_{bn} to 30 and M to 20 as a default, so that that realistic dimensions of the slopes for long-term simulations were maintained (Supplementary Figure 2).

3.3 Model scenarios and sensitivity

We assessed the effect of shoal margin collapses on the morphodynamics of a sandy estuary in three scenarios (see Table 1). We compare these scenarios with a control run without collapses to resolve the questions of how collapses affect internal channel dynamics and if collapses dynamicise the model.

The first scenario focussed on understanding the near-field effect of a single shoal margin collapse, such as the observed 2014 shoal margin collapse at the tidal flat of Walsoorden. Various sensitivity scenarios (see Supplementary Text S3) were applied to study the effect of the shoal margin collapse size, location of the collapsed deposits, and grain-size of the deposits. The sensitivity scenarios of size and location are based on the evaluation of historic collapses by *Van Dijk et al.* [2018a]. The grain size of the deposited material was varied as the grain-size distribution in the field showed minor variation between 100 μm on the shoals and 300 μm in the channel [*Mastbergen et al.*, 2016]. This scenario and sensitivity tests were conducted on only the eastern part of the Western Scheldt (see seaward boundary of model 1 in Figure 1a).

The second scenario included a model run with initially shoal margin collapses of 1,000,000 m^3 at various locations within the Western Scheldt to test the far-field effect on the sediment transport and channel-shoal dynamics over the long-term (40 years). The various locations corresponded to observed shoal margin collapse locations described in *Van Dijk et al.* [2018a] (Figure 1a).

The third scenario tested the role of multiple shoal margin collapses over a period of 40 years. These collapses were controlled by the implementation of our novel shoal margin collapse rules in a Matlab environment as described in next section. Each of the three scenarios was compared to a control run without shoal margin collapses, so that natural variation of the morphodynamics by the model could be excluded. These last two scenarios were applied on a different nested model (see Table 1), which includes the Western Scheldt from Vlissingen to the Belgian border (see seaward boundary of model 2 in Figure 1a).

3.4 Shoal margin collapses

Including the process of shoal margin collapses into a morphodynamic model might be necessary to increase internal dynamics of channel-shoal interactions. Currently, bank erosion is implemented by coupling horizontal bank retreat to bed degradation in Delft3D. Bank erosion occurs between an inundated grid cell and a dry grid cell, and thus is not restricted to the outer banks. Incision of the inundated grid cell could be equally divided over both grid cells or solely on the dry cell, so that the dry cell was lowered and the bank eroded [*Schuurman et al.*, 2016b; *Mastbergen and Schrijvershof*, 2016]. This process is continuous until the grid cell becomes inundated, but shoal margin collapses may occur suddenly at growing shoals that become less inundated.

In this study, shoal margin collapses are enforced based on the historic evaluation of collapses in the Western Scheldt and the adapted forecasting method by *Van Dijk et al.* [2018a]. The first step towards implementation is by determining the inter-tidal shoals and their margins using the method of *Leuven et al.* [2018a] by fitting a linear regression for the median bed elevation along the estuary channel. Elevation above the regression line

266 was determined as shoal and below as channel. The boundary of the shoal was then ex-
 267 tracted to determine the shoal margin. Subsequently, shoal margin collapse frequencies,
 268 F_{SC} , were calculated [adapted from *Van Dijk et al., 2018a*] as follows

$$269 \quad F_{SC} = \left[\left(\frac{H}{11} \right)^{2.5} \left(\frac{9.5}{\cot \alpha} \right)^5 \right] \frac{SC_{avg}}{L_{sm}} \quad (1)$$

270 where H is the elevation of the local maximum between the center and the deepest part
 271 within a window size of 300 by 300 m on a 20 by 20 m interpolated grid of the bed
 272 elevation. α is the corresponding angle to H , SC_{avg} is an empirical value based on the av-
 273 erage number of collapses observed per year [5.3 for the Western Scheldt, *Van Dijk et al.,*
 274 2018a], and L_{sm} is the measured total length of shoal margins [300 km for the Western
 275 Scheldt, *Van Dijk et al., 2018a*]. The form of equation 1 allowed the frequency of collapse
 276 to be greater than 1, which was prevented by a transformation, namely a Poisson process,
 277 of the frequency into a probability (P_{SC}):

$$278 \quad P_{SC} = 1 - e^{-F_{SC}} \quad (2)$$

279 *Van Dijk et al. [2018a]* found that at a probability threshold (P_{SC}) value of 10^{-4} the true
 280 positive rate, defined as the number of cells that had shoal margin collapses in both the
 281 predictive probability and observed collapses divided by the number of observed locations
 282 of collapses, was almost 0.5. While the remaining identified locations had a low false po-
 283 sitive rate, defined as the number of cells that had shoal margin collapses in the predictive
 284 probability but no observations of collapses divided by the number of cells with no shoal
 285 margin collapse observations. Because multiple locations at the shoal margin could have a
 286 probability value greater than the given threshold of 10^{-4} , we capped the number of col-
 287 lapses to a maximum of 1 per tidal flat (shoal margin) per time-interval. This means that
 288 per time-interval only a maximum of 8 collapses can occur along the Western Scheldt.
 289 The time-interval was set to 1 morphological year. Eroding shoal margins were excluded,
 290 because these were already eroding by continuous channel migration, and collapses mostly
 291 occurred suddenly at vertical aggradational margins. Eventually, the highest probability
 292 above the critical probability of 10^{-4} was used to select the location of the shoal mar-
 293 gin collapse per tidal flat. These slopes collapsed to a post-event slope whilst conserving
 294 mass, in which the size and geometric shape of the collapses followed a 1/3 ellipsoid ac-
 295 cording to the analysis of *Van Dijk et al. [2018a]* of the geometric shape of the erosion
 296 scar (see Supplementary Text S2).

297 3.5 Data analyses

298 The Delft3D model outcomes were analyzed for near-field and far-field effects, i.e.,
 299 local and estuary scale. The analysis of the near-field effects on a short-term were mainly
 300 conducted on the first scenario, whereas for the Western Scheldt model (second and third
 301 scenario) the far-field effect on the long-term morphology was analyzed. For the near-field
 302 effect we analyzed the distribution of the collapsed sediment by labelling the collapsed
 303 deposit as a second sediment fraction with the same grain-size in the model. The model
 304 outcomes were also analyzed by looking at the Digital Elevation Model (DEM) of Dif-
 305 ference (DoD) between a run with the collapse and the control run. The distribution of
 306 the collapsed sediment was plotted in a time-space diagram for the cross flow-direction
 307 as well as longitudinal flow-direction. Furthermore, the width-averaged bed elevation was
 308 calculated on the channel centerline-normal transects and compared between the runs with
 309 and without collapses.

310 For analyzing the shoal margin collapse effects, the tidally-averaged flow and mean
 311 sediment transport were calculated over a spring-neap-spring tide cycle, starting and stop-
 312 ping at the same point. Eventually, the tidally-averaged flow and mean sediment trans-
 313 port were summarized by plotting the vectors for determining the net direction of the flow

and of the sediment transport. For the second scenario, i.e., the 10 initial collapses of 1,000,000 m³, the sediment transport direction was determined for the spring-neap-spring tide cycle at the locations of the collapsed scar and associated deposit and plotted in a rose diagram. The smoothing of the bed elevation after the collapse was determined by calculating the average bed elevation within the scar and the associated deposit locations.

We were specifically interested in the role of shoal margin collapses on the channel-shoal interactions. Therefore, we used an existing network extraction tool to characterize the channel dynamics. This tool has been applied to braided rivers to determine the drainage network, so it includes channel bifurcations and confluences [Kleinhans *et al.*, 2017]. The tool uses the local lows of the channel bed to determine its lowest path. Specifically, the tool determines minimums, maximums and saddle points and connect the minimums through a saddle point, according to a descending quasi Morse-Smale complex [Kleinhans *et al.*, 2017]. Besides the lowest path, the algorithm computes a complete set of paths that form the entire channel network. To achieve this, an ordered set of non-crossing paths, known as striation, are computed. To do this, the DEM is split around the lowest path π into two parts. Then the lowest paths in those two parts of the DEM are found, and the DEM is split around these paths, and so on. This continues until a threshold, referred as a sand function (δ), is reached. The sand function is defined as the summation of the volume of sediment that has to be removed before two channels become one in the network. This volume is calculated from the elevation above the saddle point [Figure 2b Kleinhans *et al.*, 2017]. This made it possible to compute graphs representing the channel network, consisting of the lowest paths for ‘sufficiently different’ scales (Figure 2c).

Three threshold values were chosen, representing three different network scales. The networks scales are similar to the names used in the Western Scheldt [Jeuken, 2000], however, there is a mismatch between extracted channels from the network tool and field observations. The largest scale is the main channel, the next scale is referred to as the secondary channel, and the third scale is referred to as connecting channel, which in nature is the connecting channel between the main channel with the secondary channel. After identifying the channel network for the various network scales, we analyzed the channel depths for the three network scales and between model outcomes.

4 Results

4.1 The 2014 shoal margin collapse

4.1.1 Hydrodynamics

Water level changes around the shoal margin collapse location as well as around associated deposits in the channel compared to the control run as a result of the changes in bed elevation and associated bed friction. Over time, the water level fluctuates within 1 cm between both simulations under the same boundary conditions (Figure 3a, b). The main difference between the simulation with a collapse and the control run is found in the transverse direction of the collapse (Figure 3c,d & g), whereas in the longitudinal direction there is less change in the water level compared to the control run (Figure 3e, f). The largest difference in the water level change is observed at the scar of the shoal margin collapse (Figure 3d), which is inundated for a shorter time without the collapse because of the higher elevation. The water level difference between the two runs does not dominantly show lower or higher water levels around the collapse. The skewness of the change in the water level distribution indicates that water level increases for the shoal margin collapse deposit locations (Figure 3c, g), whereas the other locations show a decrease of the water level. The distribution of the water level changes varies between ebb and flood conditions for locations landward and seaward of the shoal margin collapse (Figure 3e, f), indicating

363 that water level increases for flood conditions seaward and decreases for flood conditions
364 landward.

365 Besides small changes in the water level around the collapse, we also observed small
366 changes in the tidally-averaged flow direction along the shoal margin. The control run
367 shows that the tidally-averaged flow direction (Figure 4a) is comparable with the original
368 NeVla-Delft3D model (Figure 1b) around the shoal margin of the Plaat van Walsoorden.
369 The simulation shows that the tidally-averaged flow is affected by the shoal margin col-
370 lapse, but mainly around the location of the collapse. The overall tidally-averaged flow re-
371 mains similar for both simulations but there is a slight change in direction and magnitude
372 of the tidally-averaged flow. For example, flow velocity increases along the shoal margin
373 with 0.1 m/s because of the collapse (Figure 4b).

374 **4.1.2 Sediment transport**

375 Sediment transport is calculated with the *Van Rijn* [2007a,b] equation, which sep-
376 arates the bedload from suspended load transport. The mean total transport follows the
377 direction of the tidally average flow. In the north side of the channel the total transport
378 is towards the center, whereas in the center of the channel the transport is ebb dominated
379 and south flood dominated (Figure 4c). The mean bedload transport follows the direction
380 of the tidally-averaged flow (Supplementary Figure 5a), which indicates a clear distinc-
381 tion in ebb and flood directed transport. The north side of the channel, along the shoal, is
382 mainly ebb directed, while the south side is flood directed. The mean suspended sediment
383 transport, however, does not follow the tidally-averaged flow direction at all locations, es-
384 pecially in the main channel south of the tidal flat of Walsoorden (Supplementary Figure
385 5b). Here, a direction is observed opposite from the bedload transport, in which north of
386 the channel transport is mainly flood directed, while south it is ebb directed. We suspect
387 that this is the result of the transverse bed slope predictor, which has no effect on the sus-
388 pended sediment transport.

389 The transverse bed slope of α_{bn} of 30 showed a strong transverse direction of the
390 sediment transport (Figure 4c). Additional analysis of model runs with the default α_{bn} of
391 1.5 (Supplementary Figure 5d) showed that the magnitude in the longitudinal direction is
392 comparable. This understanding is essential regarding the migration of the perturbation
393 of the shoal margin collapse through the channel of the estuary. Because of the change in
394 the tidally-averaged flow due to the shoal margin collapse, the sediment transport direc-
395 tion and magnitude is affected as well. For example, the run with the shoal margin col-
396 lapse of 2014, the mean total transport, i.e., the effective sediment transport, reduces by
397 a value that is 80% of the mean total transport for the control run at the location where
398 sediment from the collapse deposited (Figure 4d). The mean total transport, however, in-
399 creases along the shoal margin by 15% and especially increases within the shoal margin
400 collapse. Less sediment transport means that erosion of the deposited sediment will take
401 longer, whereas the increase in sediment transport would increase erosion along the shoal
402 margin.

403 **4.1.3 Morphodynamics**

404 By comparing the run with the 2014 shoal margin collapse scar and deposit with the
405 control run, changes in the morphology between the runs can be ascribed specifically to
406 the shoal margin collapse because the natural variation in the morphology was excluded.
407 The DEM of difference (DoD) shows that the bed elevation in the channel landward as
408 well as seaward of the collapsed deposit is raised after about 1 year of morphological
409 time, whereas the location of the deposit is lowered from the start of the simulation (Fig-
410 ure 4e). This suggests smoothing of the profile after the collapse. The shoal margin col-
411 lapse scar is still visible as it remains lower compared to the control run, and the process
412 of sedimentation is slower compared to the erosion that smooths the channel.

413 The difference in bed elevation shows the changes between the two runs, but does
 414 not show how sediment from the collapse is distributed. Therefore, in the simulation with
 415 the 2014 shoal margin collapse the collapsed sediment is labelled, so that the spreading
 416 of the sediment could be traced. Figure 4f shows the distribution of the sediment from
 417 the collapse within the main channel at the *Plaat van Walsoorden*. Large portions are de-
 418 posited at the sides of the original location, which corresponds with the DoD. The distri-
 419 bution of the collapsed sediments is spread over a larger area in the landward as well as
 420 seaward direction, which is less clear from the DoD because of the limited changes in bed
 421 elevation. Suspended sediment is supposed to travel a longer distance leading to distribu-
 422 tion over a larger area, whereas bedload sediment affected the bed elevation more. Despite
 423 the transport in both directions there is a dominant distribution of the tracer sediment in
 424 ebb direction (Figure 4f).

425 4.2 Shoal margin collapse scenarios to determine sensitivity

426 In the supplementary we elaborate more in detail regarding the sensitivity of various
 427 scenarios, such as the size of the collapse, the location of the collapsed sediment and the
 428 role of grain-size. The results from this analysis is that the migration rate of the distur-
 429 bance is hardly affected by the collapsed volume, and that only large collapses, $> 100,000 \text{ m}^3$
 430 affect the far-field channel-shoal interactions (Supplementary Figure 7). This is mainly be-
 431 cause the volume of collapsed material is relatively small compared to the characteristic
 432 shoal volume of 34 million m^3 . The location of the collapsed deposits along the Western
 433 Scheldt determines the dominant direction of the disturbance, which corresponds to the
 434 tidally-averaged flow direction. Collapses that occurred more landwards are less reworked
 435 and the transport direction is dominantly in seaward direction (Supplementary Figure 7).
 436 Model outcomes for different α_{bn} values do not change longitudinal displacement of the
 437 disturbance but do effect the distribution of the sediments in transverse direction (Sup-
 438 plementary Figure 5c, d). Alongside the location of the collapsed deposit, the grain-size
 439 of the deposit also determines the direction of the disturbance. Finer material follows the
 440 same dominant longitudinal direction as the $200\mu\text{m}$, but more sediment is deposited at the
 441 sides of the channel. Coarse material is, however, primarily transported in the strongest
 442 flow direction rather than that of the tidally-averaged flow, so that only the sediment in the
 443 deepest part of the channel is entrained (Supplementary Figure 6).

444 To summarize, shoal margin collapse scars and associated sediment deposits in the
 445 channel locally affect the dynamics of the Western Scheldt affecting sediment transport di-
 446 rection and morphology within the first year after occurrence. Additionally, the size and
 447 location of the collapse have direct effects on the magnitude and direction of these dynam-
 448 ics.

449 4.3 Shoal margin collapses in the Western Scheldt

450 The 2014 shoal margin collapse is one of the larger collapses that occurred but its
 451 isolated effect on the estuary morphodynamics is limited. Here, we first assess how much
 452 effect each individual location susceptible to collapse (see specific collapsed locations in
 453 Supplementary Figure 4a) has on the morphodynamics, and then apply our novel shoal
 454 margin collapse method to test if multiple yearly collapses over time would dynamicise the
 455 Western Scheldt estuary.

456 4.3.1 Multiple initial collapses

457 The Western Scheldt schematization (model 2) is used to test the long-term effect
 458 of multiple shoal margin collapses on the morphodynamics of the system for 40 years.
 459 In the first scenario, 10 shoal margin collapses of a volume of $1,000,000 \text{ m}^3$ are initially
 460 added to the bed elevation of the Western Scheldt. Examining the sediment transport di-
 461 rection for the various locations shows that sediment transport direction and rate varies

with location. Most locations show sediment transport in two dominant directions corresponding with the ebb and flood current, in which dominant direction can differ between the source (scar) and the associated sediment deposit (Figure 5). Furthermore, at most locations the sediment transport is less for the location of the scar where the collapse originated compared to the location where it deposited. This is particularly true for more landward scars, which typically are shallower, and the surrounding area becomes dry during low tide. There are some exceptions to this, where the collapse occurs under water, e.g., the Spijkerplaat (location A), and the scar remains fully under water during the tidal cycle. Perpendicular to the ebb and flood flow sediment is transported on the transverse bed slope, probably because of the relative high α_{bn} of 30, a strong perpendicular vector is observed, which is specifically true for the collapse at the Molenplaat and Plaat van Walsoorden (locations F and I).

The sediment transport magnitude determines the rate that the shoal margin collapse is filled and the associated collapsed sediment is eroded from the main channel. The net sediment transport varies between ebb and flood flow as well as between spring and neap tidal cycles. The net sediment transport for neap tidal cycle is about $5 \cdot 10^5 \text{ m}^3$ and for spring tidal cycle about $5 \cdot 10^6 \text{ m}^3$ within the Western Scheldt estuary. The net sediment transport is slightly higher during rising tide than for falling tide. Locations with the highest sediment transport rates, such as the Spijkerplaat West and Ossensisse (locations A and H), show faster infilling of the shoal margin collapse (Figure 6a). The collapse at the Plaat van Walsoorden (location I) is less filled, which is also observed for the first scenario model outcome, and can be associated to lower sediment transport rates. The rate of infilling and erosion deviates from the 2014 collapse observations, and are generally less, especially for filling of the scar (Figure 6a). Sediment transport rate also determines the rate of erosion of the collapsed sediment. In general, the erosion is faster than the infilling except for the deposits in the secondary channels (Figure 6b), e.g., the Brouwersplaat (E) and Molenplaat (F).

The initial collapses affect the long-term changes of the morphology in the estuary. The bed elevation difference and tracer sediment distribution map (Figure 7a) indicate that shoal margin collapses perturb the Western Scheldt differently depending on their location, which corresponds to the sediment transport direction and magnitude at the collapsed locations (Figure 5). Major changes in bed elevation are observed around the shoal margin collapse locations (Figure 7a), as sediment is distributed in landward and seaward direction from its original location. Interesting effects are observed when the disturbances enter areas that have less sediment transport but are morphodynamically active and controls sediment diversion, i.e., the junctions seaward or landward of the channel. Here, the bed elevation is not only affected in the longitudinal direction but also in the transverse direction into connected channels (Figure 7a), i.e., effectively following the sediment vectors. For example, the collapse at location B changes the bed morphology of both landward channels compared to the control run, which also appear at the landward direction of location H (Figure 7a).

On a longer timescale, the shoal margin collapses affect the dynamics of the system, so that a total volume change of $4.53 \cdot 10^8 \text{ m}^3$ was observed compared to the control run, in which less than 10% of the volume is directly the result of the collapses. The width-averaged mean bed level difference between the two simulations shows that changes excite, i.e., grow, over time (Figure 7b). At the beginning, there is a slight difference between the runs, which was also demonstrated with the 2014 collapse, but eventually the mean bed elevation between the two simulations varies more than a meter (Figure 7b). This is primarily the result of migration of the junction around location C and landward of location H (Figure 7a). The sediment from the shoal margin collapse is mainly transported in the longitudinal direction, landward as well as seaward (Figure 7a). Following the tracer sediment along the estuary gives more insights in the dominant migrating direction of the disturbance (Figure 7c), which vary with location but is dominantly landwards for the

515 seaward collapses and seawards for the more landward collapses (following the dominant
 516 direction shown in Figure 5). Changes in the bed elevation even occur on the locations
 517 where no sediment is located that originates from shoal margin collapse, e.g., at 25 km,
 518 which is at one of the channel junctions (Figure 7b,c).

519 **4.3.2 Multiple yearly collapses**

520 In the third scenario, shoal margin collapses are added after each morphological
 521 year. The shoal margin collapses vary in size and location according to the given rules
 522 (see method section). Over a 40 year simulation 227 collapses occurred, i.e., 5.7 per year,
 523 at 58 independent locations of distinct tidal flats (illustrated by contour lines in Figure 8a),
 524 eroding a total volume of 40 million m³, i.e., 1 million m³ per year, which total volume
 525 is more than the historic field observations. As shown in previous scenarios the distribu-
 526 tion of the disturbance varies with location depending on flow conditions (see direction
 527 in Figure 1b-e), showing mainly changes in the bed elevation in the longitudinal direc-
 528 tion, i.e., landward and seaward of the collapse (Figure 8a). Collapses near the junctions
 529 lead to changes in the bed elevation across the channel because the channel is wider and
 530 shallower. This typically occurred at the same locations (B and H) as for the initial col-
 531 lapses, and bed elevation differs up to 10 m compared to the control run. The total bed
 532 volume difference at the end of the model run compared to the control run is $4.63 \cdot 10^8$ m³,
 533 in which 20% of the volume is directly explained by the shoal margin collapses.

534 The width-averaged bed level difference between the run with collapses and the control
 535 run (Figure 8b) illustrates migration of the disturbance in both directions, excitation
 536 of the disturbance over time and also dampening of the disturbance. The bed elevation
 537 difference is dampen for the collapses that occurred at 13 m from the seaward end (Fig-
 538 ure 8b), whereas migration is detected at 28 km from the seaward end (Figure 8b). Fur-
 539 thermore, there are some unexplained responses that are not directly associated with the
 540 collapses itself, such as observed between 25 and 37 km from the Western Scheldt mouth,
 541 which probably originated is due to excitation of earlier collapses(Figure 8b). Because of
 542 the number of collapses and the yearly adding of new collapses, the effect of a single dis-
 543 turbance is difficult to follow. Most changes occur at the locations with several collapses.
 544 Because of boundary effects at the seaward side, we excluded the seaward effects for fur-
 545 ther interpretation and conclusions of the role of shoal margin collapses as this might be
 546 associated to the boundary and not to actual collapses. The total eroded and deposited
 547 volume is $2.31 \cdot 10^9$ m³ for the run with collapses and $2.26 \cdot 10^9$ m³ for the control run,
 548 which suggest the simulation are equally dynamic as only 10.0 million m³ of the eroded
 549 volume is not explained by the collapsed volume of 40 million m³.

550 **4.4 Re-organization of the channel-shoal network by collapses**

551 The addition of yearly collapses in the model leads to changes in the network struc-
 552 ture and the scale at which channels are detected as compared to the control run (Fig-
 553 ure 9a, b). While the main channel location and scale are generally the same between
 554 the three runs over time (Supplementary Figure 8), many of the smaller scale channels
 555 are identified differently for the model run with yearly collapses. In the control run, less
 556 smaller scale channels, i.e. secondary and connecting, are observed compared to the run
 557 with yearly collapses (Figure 9a-b), which means there is better connectivity among the
 558 channels for the model with yearly collapses. The scale, or sand function volume, at which
 559 channels are detected, changes between the runs as well. The shifting of scale is due to
 560 the differences in the morphological development of the system. In the case of the col-
 561 lapses, the secondary channel network shifts (Figure 9b), probably because of sediment
 562 deposition in the channel which decreases the volume of sediment between adjacent chan-
 563 nels, causing channels that were identified as secondary in the control run to be identi-
 564 fied as connecting channels in the run with collapses. Over time, the location of the main
 565 channel associated to channel migration, covers 2% less of the Western Scheldt for the

yearly collapses, whereas the secondary channel covers 4% more of the Western Scheldt in the situation with yearly collapses (Supplementary Figure 8).

The various channel networks are used to determine the depth distribution of the channels. The initial network shows a deep main channel (Table 2, Figure 9c) probably due to the dredging activities for maintaining a specific depth of the shipping fairway in the Western Scheldt. After 40 years of morphological development, the main channel becomes deeper but the variation increases (Table 2), showing deeper but also shallower channels. There is an increase in the number of smaller scale channels (Figure 9d), especially for the run with yearly collapses (Figure 9f). Although, we observed some changes in bed elevation between the control run and the model run with initial 10 collapses (Figure 7), the bed elevation for the largest scale of the network is comparable (Figure 9d,e). Major changes are observed between the secondary and connecting scale channels, the number of connecting scale channels increases for the run with initial collapses, while the depth generally decreases. The depth of the secondary channel, however, increases for the run with initial collapses. The system with yearly collapses develops to a system with shallower channels because of collapses occur mainly in the main-channel. The secondary channels approaches the same depth distribution as the main channel on the long-term, whereas the number of connecting channels increases (Figure 9f).

5 Discussion

We introduced an effective parametrization for the process of shoal margin collapse, based solely on the local bed elevation and slope gradient. Here, we discuss how the response of the modeled collapses affects the morphodynamics and how this differs from observations. We also consider the implication of shoal margin collapses on perturbing the channel-shoal interactions and hypothesize these compare to larger perturbations caused by dredging and disposal activities.

5.1 Modeled collapses versus observations

The 2014 shoal margin collapse is used to test the near-field effects of a shoal margin collapse. This collapse is well studied by *Van Schaick* [2015] by analyzing field measurements and Delft3D simulations. *Van Schaick* [2015] concluded that some morphodynamics of the model differ from the observations [*Mastbergen et al.*, 2016]. According to field measurements, sediment deposited from the shoal margin collapse migrated in the flood direction, i.e., flood-directed net bedload, while the model outcome suggests ebb-directed net bedload. The discrepancy in the net bedload direction could be explained by the inaccuracy in the modeled hydrodynamics. The collapsed deposit from the 2014 shoal margin collapse is located in that part of the channel where tidally-averaged flow is ebb dominated but almost zero, whereas south from the deposit the tidally-averaged flow and mean sediment transport suggest transport in the flood direction. However, the flood current is generally stronger in the channel, which might have led to distribution of the deposit in the flood direction instead of the modeled ebb direction. The rate of infilling of erosion scars was less in the model compared to field observations (Fig 6a), whereas the field observation of erosion of the associated deposit compares more closely to the modeled results. The difference indicates that the model has difficulties with simulation of the shallower regions, maybe because no extreme water level conditions are included (only 1 repeated month of real time-series) nor combined astronomical and meteorological forces [*De Vet et al.*, 2018]. Additionally, filling of the scars increases when mud fraction is added to the model [*Van Schaick*, 2015].

The shoal margin collapse parametrization leads to several collapses along the Western Scheldt Estuary. The location is based on the bed elevation, such that steep slopes collapse, whereas the collapsed size and volume is randomly drawn from a log-normal distribution. Locations for shoal margin collapses (Figure 8a) do vary from the observed lo-

616 cations (Figure 1a), probably because for the chosen probability threshold value the num-
617 ber of false positives is at least equal to the true positives, meaning that steep high slopes
618 that are not susceptible to collapses are included [Van Dijk *et al.*, 2018a]. Nonetheless, the
619 collapses are widely distributed on tidal flats that do have collapses over time. Locations
620 with rapid infilling of the scar relates to locations with multiple collapses, e.g., at Spijker-
621 plaat (location A) and Ossensisse [location H, Van Dijk *et al.*, 2018a]. Our parametrization
622 differs from earlier attempts to prevent steep slopes of bars in rivers with Delft3D [Nieuw-
623 boer, 2012]. Nieuwboer [2012] applies two strategies to reduce steep slopes in Delft3D;
624 1) slope avalanching, and 2) slope slumping, in which avalanching stopped deposition
625 of sediment on steep slopes and slumping leads to changing steep slopes to equilibrium.
626 The slope slumping, however, leads to numerically unstable simulations because of large
627 changes in the water levels. Here, no numerical instabilities were observed, because the
628 collapses mainly occurred underwater and water depths are higher in the estuary setting
629 compared to shallow rivers. Furthermore, sediment was not deposited in adjacent cells but
630 spread in the deeper parts of the channel following the slope of the collapsed shoal.

631 Our parametrization is, however, limited in the prediction of the collapses as the
632 original probability prediction of Van den Ham *et al.* [2014] includes also variables for
633 sediment properties, such as grain-size, relative density and the amount of mud layers
634 [Mastbergen and Van den Berg, 2003], whereas we solely calculated with uniform sedi-
635 ment size. These variations in sediment properties are formed when the channels mi-
636 grate, forming new shoals on the inner banks whilst collapsing outer banks retreat into
637 the layer-cake of sand and mud of past shoals and marshes [Dalrymple and Rhodes, 1995;
638 Van den Berg *et al.*, 1996; Fagherazzi *et al.*, 2004]. Spatial information of the stratigraphy
639 is, however, lacking for most systems because the limited availability of field data. Even
640 for the well-studied Western Scheldt a model is used to predict clay availability within the
641 tidal flats [Dam, 2017], but lacks the detailed information. The applied Western Scheldt
642 schematization includes only a single fraction, but it will be of interest for future studies
643 to calculate with multiple fractions, especially to construct a subsurface including varia-
644 tions in sediment properties, e.g., mud [Braat *et al.*, 2017].

645 **5.2 Implications of shoal margin collapse perturbations on the morphodynamics**

646 The rate of sediment removal and the volume of a single collapse determine the
647 channel dynamics around the collapse. In the less dynamic secondary channels, the sedi-
648 ment is less spread, so that the collapse has less impact on the channel-shoal interactions.
649 Small collapses can be seen as noise to the system, while larger collapses can be seen as
650 a perturbation of the system [Kleinhans *et al.*, 2015]. The shoal margin collapse firstly
651 affects the local bed elevation by depositing sediments into the main channel, but over
652 time this disturbance propagates through the channel network. The findings correspond
653 partly with the conceptual model described by Schuurman *et al.* [2016a] for disturbances
654 in braided rivers. In the estuary, however, an adjustment in the channel leads to adjust-
655 ments in the downstream and upstream directions. The dominant direction depends on
656 whether the channel is ebb- or flood-dominant. The migration rate is low for the distur-
657 bance but larger than changes of the shoals (tidal flats) themselves, which are more or less
658 fixed at their location [Leuven *et al.*, 2018b].

659 The initial 10 collapses show that the perturbations lead to excitation of the differ-
660 ence in bed elevation compared to a control run on the long-term (Figure 7). Specifically,
661 the bed elevation difference between the runs increases rapidly after 20 years. After 40
662 years of morphological development, the modeled bed elevation difference between the
663 control run and the run with initial collapses is only explained by less than 10% of the
664 initial collapsed volume. In the case for the scenario with yearly collapses, the modeled
665 bed elevation difference (Figure 8) is explained by 20% of the collapsed volume, probably
666 this percentage is less because the effect from the disturbances are still growing, the per-
667 turbations are less effective because of some smaller collapses, or small perturbations are

668 overprinted by larger ones. In the case of the initial collapses, the perturbation grows over
669 time but besides some deepening of the secondary channel the channel network remains
670 the same. On the other hand, the yearly collapses change the course of the secondary and
671 main channel at a few locations (Supplementary Animation 1).

672 Shoal margin collapses perturb the estuary differently depending on the location of
673 the collapse within the channel network. In general, the shoal margin collapses change
674 the channel-shoal network by shallowing of the major channels and forming new smaller
675 channels on the tidal flats. The network tool provides a network at the final timestep (Fig-
676 ure 9), illustrating the overall changes between the control run and the yearly collapse but
677 did not illustrate changes that can be linked to the collapses themselves. Analysis of the
678 channel depth for the various scales in time shows that the variation in channel depth
679 increases in time, except for the secondary channels (Figure 10). The channel network
680 changes part of the main channel into the secondary channel within the first 5 years for
681 all runs, so that the secondary channel deepens and the main channel becomes shallower
682 (Figure 10a, b). The collapses in the scenario with yearly collapses mainly affect the sec-
683 ondary and connecting scale channel networks, which deviates from the control run (Fig-
684 ure 10b, c). A few collapse events can be directly related with changes in the channel net-
685 work depth. For example, the collapses in year 22 results in shallowing of the secondary
686 scale channel (Figure 10b). Changes in the depth of the main and secondary channel net-
687 work scales are not always directly affected by the collapses but might be the result of
688 multiple collapses that affected the connecting scale channel networks. For example, the
689 shallowing of the secondary scale channel network after 10 years corresponds to a deep-
690 ening of the connecting scale channel network that occurred a year before (Figure 10b,
691 c).

692 The shoal margin collapses do not dynamicise the model as we hypothesized, but
693 do affect the estuary channel-shoal interaction compared to a control run without col-
694 lapses. The most interesting responses from the collapses on the channel-shoal interac-
695 tions are observed near junctions (sills, Figures 7-8), corresponding to the overlapping
696 sediment circulation cells [Wang *et al.*, 1995]. Here, there is less gross sediment trans-
697 port but the channels shift more often than other parts of the Western Scheldt [Van Dijk
698 *et al.*, 2018a]. This is observed from the DEM of differences for the last decades [Gras-
699 meijer *et al.*, 2013], whereas analysis of the development of channel-shoals in the West-
700 ern Scheldt shows overall a more dynamic system for the period 1860-1955 [Dam, 2017].
701 These field observations suggest that dynamics of the shoals have decreased in the last
702 decades and that perturbations, such as shoal margin collapses, are efficiently removed in
703 the main and secondary channels and therefore only affect the development at the shal-
704 lower sills and channel junctions. The mean bed elevation at the junction does increase
705 even when there is almost no direct deposition of the collapsed sediment (Figure 7b, c).
706 A reason could be that collapsed sediment is spread over a larger/wider distance, however
707 the role of the junction is significant as this leads to excitation of the disturbance. Dis-
708 turbances at the junction change the flow direction towards the successive shoal, like the
709 successive bifurcation in a braided river [Schuurman *et al.*, 2016a], but also the flow direc-
710 tion towards the shoal itself as the tidally-averaged flow circulates, i.e., marco cell, around
711 the shoal (Figure 1b). This means that disturbances near a junction would have a larger
712 effect on the channel-shoal interactions. For example, the collapses near Borssele (loca-
713 tion B) and at Ossennisse (location H) result in larger differences from the control run. In
714 the field, however, these junctions (sills) are well managed as this is part of the shipping
715 fairway, and therefore its depth is maintained by dredging activities [Verbeek *et al.*, 1998],
716 which means that the role of collapses are interrupted in the field.

717 The role of the shoal margin collapses might affect the estuary differently com-
718 pared to dredging and disposal activities, which is conducted to deepen the main channel.
719 In this study, we have not included dredging and disposal, which would affect our find-
720 ings. Dredging activities at the toe of the Platen van Ossennisse [Drempel van Hansweert

721 *Groenewoud, 1997*] might lead to deepening and increase the number of shoal margin
722 collapses in the field, which is not included in our simulations. Analysis from disposal
723 strategies also showed that disposal of sediment in the secondary channels takes longer to
724 spread, because of lower sediment transport, and forms a threat for the existence of the
725 multi-channel network [*Meersschaut et al., 2004*]. Dredged volumes are 10 times larger
726 compared to the volume of shoal margin collapses in the Western Scheldt, and we would
727 argue, therefore, that the role of shoal margin collapses on the morphodynamics in the
728 Western Scheldt is hardly observable. But this study shows that collapses do play a role in
729 the more local, meso-scale morphology, e.g. additional channel-shoal interaction leading
730 to more dynamics. It will be of interest to test the effect on the long-term channel network
731 due to dredging-disposal disturbances and its stability of the multiple channel network
732 [*Wang, 2015*].

733 **6 Conclusions**

734 Detailed analysis of the large 2014 shoal margin collapse shows that the hydrolog-
735 ical and morphological processes around the collapse affects both water levels and the
736 sediment transport direction. Model results show that single shoal margin collapses only
737 affect the local dynamics in the longitudinal direction and dampen out within a year when
738 volumes are small. The extent of far-field effects is sensitive to the grain-size of the de-
739 posit, where finer sediments are transported further away and settle on the sides of the
740 channel while larger grains are hardly entrained and only eroded during the stronger flood
741 flow. The distribution of the collapsed sediment deposit across the channel disturbs the
742 region around the collapse, where sediment transport is dominantly following the tidally-
743 averaged flow but coarser sediment follows the stronger flood flow. The perturbation by
744 the shoal margin collapses increases channel migration rate, as the deposited sediment
745 pushes the flow against the banks. These results imply that disturbances caused by dredg-
746 ing and dumping may likewise affect the dynamics of channel junctions as well, because
747 dredging volumes are at least 10 times larger than the collapsed volumes.

748 We presented a parametrization for shoal margin collapses and coupled this to the
749 Delft3D model, so that effects of multiple yearly collapses of various sizes on the mor-
750 phodynamics could be tested. We found that near-field morphodynamics in the channel
751 are slightly affected at a timescale of a year due to increasing bed elevation and chang-
752 ing water levels, but far-field effects controlled by processes such as the tidally-averaged
753 flow vectors are negligible affected by the collapses. When larger disturbances reach the
754 seaward or landward junction at tidal channel junctions over a longer time span, the bed
755 elevation at the junction increases on average and decrease the hydraulic geometry of the
756 channel junctions. Here, the perturbation affects the morphology in the longitudinal as
757 well as transverse direction, and affect the channel network on a longer term when the
758 flow and sediment distributions into the multiple channels are shifted. The initial collapses
759 have no effect on the long-term channel-shoal morphodynamics, although only 10% of bed
760 elevation difference is explained by the collapsed volume. The yearly collapses resulted
761 in a shallowing of the main channel as they mostly occur along the main channel, and
762 change the channel networks at the various scales. The secondary scaled channels become
763 deeper, whereas the number of the connecting scale channels increases when the system
764 becomes generally shallower. We conclude that multiple yearly collapses are changing the
765 channel-shoal morphodynamics in estuaries, but that the role of the collapses is limited for
766 heavily dredged systems such as the Western Scheldt. On the other hand, estuaries that are
767 not intensively dredged may not develop oversteepened bar margins with frequent shoal
768 margin collapses.

769 **Acknowledgments**

770 WMvD and MGK were supported by the Dutch Technology Foundation TTW (grant STW-
771 Vici-016.140.316/13710 to MGK), which is part of the Netherlands Organisation for Sci-

entific Research (NWO). MH and MGK were supported by the European Research Council (ERC Consolidator agreement 647570 to MGK). We gratefully acknowledge Marco Schrijver (Rijkswaterstaat), Dick Mastbergen, Marcel Taal (Deltares), Jelmer Cleveringa (Arcadis) and Yves Plancke (WL Antwerpen) for insightful discussions. We greatly thank Willem Soncke, Tim Ophelders, Kevin Verbeek and Bettina Speckman of TU Eindhoven for providing the network extraction tool. Constructive and positive reviews by Ioannis Georgiou, Travis Swanson and one anonymous reviewer, Associate Editor Ton Hoitink, and Editor Giovanni Coco helped to clarify and strengthen the manuscript. The data used are reported in the references, figures and supporting information. The code for shoal margin collapses is available on the online GitHub repository [Van Dijk *et al.*, 2018b].

References

- Ahktar, M. P., N. Sharma, and C. S. P. Ojha (2011), Braiding process and bank erosion in the Brahmaputra River, *International Journal of Sedimentary Research*, 26, doi: 10.1016/S1001-6279(12)60003-1.
- Ashworth, P. J., and J. Lewin (2012), How do big rivers come to be different?, *Earth-Science Reviews*, 114, 84–107, doi:10.1016/j.earscirev.2012.05.003.
- Baar, A., M. B. Albernaz, W. Van Dijk, and M. Kleinhans (2018a), The influence of transverse slope effects on large scale morphology in morphodynamic models, in *Riverflow 2018*, vol. 40, doi:10.1051/e3sconf/20184004021, cited By 0.
- Baar, A. W., J. De Smit, W. S. J. Uijtewaal, and M. G. Kleinhans (2018b), Sediment transport of fine sand to fine gravel on transverse bed slopes in rotating annular flume experiments, *Water Resources Research*, p. 10.1002/2017WR020604.
- Baeyens, W., B. van Eck, C. Lambert, R. Wollast, and L. Goeyens (1997), General description of the scheldt estuary, *Hydrobiologia*, 366(1), 1–14, doi: 10.1023/A:1003164009031.
- Bagnold, R. (1966), *An approach to the sediment transport problem from general physics*, U.S. Geol. Survey. Prof. Paper 422-I.
- Beinssen, K., D. T. Neil, and D. R. Mastbergen (2014), Field observations of retrogressive breach failure at the two tidal inlets in Queensland, Australia, *Australian Geomechanics*, 49(3), 55–64.
- Bolle, A., Z. B. Wang, C. Amos, and J. De Ronde (2010), The influence of changes in tidal asymmetry on residual sediment transport in the Western Scheldt, *Continental Shelf Research*, 30, 871–882, doi:10.1016/j.csr.2010.03.001.
- Braat, L., T. Van Kessel, J. R. F. W. Leuven, and M. G. Kleinhans (2017), Effects of mud supply on large-scale estuary morphology and development over centuries to millennia, *Earth Surface Dynamics Discussion*, 5, 617–652, doi:10.5194/esurf-5-617-2017.
- Cancino, L., and R. Neves (1999), Hydrodynamic and sediment suspension modelling in estuarine systems, *Journal of Marine Systems*, 22, 117–131, doi:10.1016/S0924-7963(99)00036-6.
- Canestrelli, A., A. Spruyt, B. Jagers, R. Slingerland, and M. Borsboom (2016), A mass-conservative staggered immersed boundary model for solving the shallow water equations on complex geometries, *International Journal for Numerical Methods in Fluids*, 81, 151–177, doi:10.1002/flid.4180.
- Coleman, J. M. (1969), Brahmaputra River: channel processes and sedimentation, *Sedimentary Geology*, 3, 129–239, doi:10.1016/0037-0738(69)90010-4.
- Crosato, A., and M. S. Saleh (2011), Numerical study on the effects of floodplain vegetation on river planform style, *Earth Surface Processes and Landforms*, 36, 711–720.
- Dalrymple, R., and R. Rhodes (1995), Estuarine dunes and bars, in *Developments in Sedimentology*, vol. 53, pp. 359–422, Elsevier, New York, doi:10.1016/S0070-4571(05)80033-0.
- Dam, G. (2013), Harde lagen Westerschelde (in Dutch), *Tech. rep.*, International Marine & Dredging Consultants.

- 824 Dam, G. (2017), Lange-termijn sedimentbalans Westerschelde (in Dutch), *Tech. rep.*,
825 SVASEK hydraulics.
- 826 Darby, S. E., A. M. Alabyan, and M. J. Van de Wiel (2002), Numerical simulation of
827 bank erosion and channel migration in meandering rivers, *Water Resources Research*,
828 38, doi:10.1029/2001WR000602.
- 829 De Vet, P. L. M., B. C. Van Prooijen, R. A. Schrijvershof, J. J. Van der Werf, T. Ysebaert,
830 M. C. Schrijver, and Z. B. Wang (2018), The importance of combined tidal and me-
831 terological forces for the flow and sediment transport on intertidal shoals, *Journal of*
832 *Geophysical Research – Earth Surface*, doi:10.1029/2018JF004605.
- 833 De Vriend, H. J., Z. B. Wang, T. Ysebaert, P. M. J. Herman, and P. Ding (2011), Eco-
834 morphological problems in the Yangtze Estuary and the Western Scheldt, *Wetlands*, 31,
835 1033–1042, doi:10.1007/s13157-011-0239-7.
- 836 Deltares (2009), *Delft3D-FLOW User Manual, Simulation of Multi-Dimensional Hydro-*
837 *dynamic Flows and Transport Phenomena, Including Sediments*, Deltares, Delft, The
838 Netherlands.
- 839 Dunbar, J. B., V. H. Torrey, and L. D. Wakeley (1999), A case history of embankment
840 failure: geological and geotechnical aspects of the Celotex levee failure, New Orleans,
841 Louisiana, *Technical report*, US Army Corps of Engineers, Vicksburg, Mississippi,
842 USA.
- 843 Fagherazzi, S., E. J. Gabet, and D. J. Furbish (2004), The effect of bidirectional flow on
844 tidal channel planforms, *Earth Surface Processes and Landforms*, 29, 295–309, doi:
845 10.1002/esp.1016.
- 846 Grasmeyer, B., G. Dam, and M. Taal (2013), Actualisatierapport Delft3D Schelde-
847 estuarium (in Dutch), *Tech. rep.*, International Marine & Dredging Consultants.
- 848 Groenewoud, M. D. (1997), Modelling morfodynamisch gedrag van de Drempel van
849 Hansweert (in Dutch), Master's thesis, TU Delft.
- 850 Gruijters, S. H. L. L., J. Schokker, and J. G. Veldkamp (2004), Kartering moeilijk erodeer-
851 bare lagen in het Schelde estuarium (in Dutch), *rapport NITG 03213B1208*, TNO.
- 852 Ikeda, S. (1982a), Incipient motion of sand particles on side slopes, *Journal of Hydraulics*
853 *Division*, 108(1), 95–114.
- 854 Ikeda, S. (1982b), Lateral bed load transport on side slopes, *Journal of Hydraulics Divi-*
855 *sion*, 108(11), 1369–1373.
- 856 Jerolmack, D. J., and C. Paola (2010), Shredding of environmental signals by sediment
857 transport, *Geophysical Research Letters*, 37(19), doi:10.1029/2010GL044638, 119401.
- 858 Jeuken, M. C. J. L. (2000), On the morphologic behaviour of the tidal channels in the
859 Westerschelde estuary, Ph.D. thesis, Universiteit Utrecht.
- 860 Khan, N. I., and A. Islam (2003), Quantification of erosion patterns in the Brahmaputra-
861 Jamuna River using geographical information system and remote sensing techniques,
862 *Hydrological Processes*, 17, doi:10.1002/hyp.1173.
- 863 Kleinhans, M. G. (2010), Sorting out river channel patterns, *Progress in Physical Geogra-*
864 *phy*, 34, 287–326, doi:10.1177/0309133310365300.
- 865 Kleinhans, M. G., C. Braudrick, W. M. Van Dijk, W. I. Van de Lageweg, R. Teske, and
866 M. Van Oorschot (2015), Swiftness of biomorphodynamics in Lilliput- to Giant-sized
867 rivers and deltas, *Geomorphology*, 244, 56–73, doi:10.1016/j.geomorph.2015.04.022.
- 868 Kleinhans, M. G., M. Kreveld, T. Ophelders, W. Sinke, B. Speckmann, and K. Verbeek
869 (2017), Computing representative networks for braided rivers, in *33rd International Sym-*
870 *posium on Computational Geometry (SoCG 2017), Leibniz International Proceedings*
871 *in Informatics (LIPIcs)*, vol. 77, edited by B. Aronov and M. J. Katz, pp. 48:1–48:16,
872 Schloss Dagstuhl–Leibniz-Zentrum fuer Informatik, doi:10.4230/LIPIcs.SoCG.2017.48.
- 873 Laury, R. L. (1971), Stream bank failure and rotational slump: preservation and signifi-
874 cance in the geologic record, *Geological Society of America Bulletin*, 82, 1251–1266.
- 875 Leuven, J. R. F. W., T. De Haas, L. Braat, and M. G. Kleinhans (2018a), Topographic
876 forcing of tidal sand bar patterns for irregular estuary planforms, *Earth Surface Pro-*
877 *cesses and Landforms*, 43(1), 172–186, doi:10.1002/esp.4166.

- 878 Leuven, J. R. F. W., L. Braat, W. M. van Dijk, T. De Haas, J. Cleveringa, and M. G.
879 Kleinhans (2018b), Growing forced bars determine non-ideal estuary planform, *Earth-*
880 *ArXiv*, doi:10.17605/OSF.IO/HJ27M.
- 881 Mastbergen, D. R., and R. Schrijvershof (2016), Sedimentatiepatronen Plaat van Walsoor-
882 den na plaatval 22 juli 2014 (in Dutch), *Tech. rep.*, Deltares, deltares.
- 883 Mastbergen, D. R., and J. H. Van den Berg (2003), Breaching in fine sands and the gener-
884 ation of sustained turbidity currents in submarine canyons, *Sedimentology*, 50(4), 625–
885 637, doi:10.1046/j.1365-3091.2003.00554.x.
- 886 Mastbergen, D. R., G. A. Van den Ham, M. Cartigny, A. Koelewijn, M. De Kleine,
887 J. Hizett, M. Azpiroz, and A. Vellinga (2016), Multiple flow slide experiment in the
888 Westerschelde Estuary, The Netherlands, in *Submarine Mass Movements and Their Con-*
889 *sequences, 7th Int. Symp, Advances in Natural and Technological Hazards Research*,
890 vol. 41, edited by G. Lamarche, J. Mountjoy, S. Bull, T. Hubble, S. Krastel, E. Lane,
891 A. Micallef, L. Moscardelli, C. Mueller, I. Pecher, and S. Woelz, pp. 241–249, Springer
892 International Publishing, Wellington, New Zealand, doi:10.1007/978-3-319-20979-1.
- 893 Maximova, T., S. Ides, J. Vanlede, T. De Mulder, and F. Mostaert (2009a), Verbetering 2D
894 randvoorwaardenmodel. Deelrapport 3: kalibratie bovenlopen (in Dutch), *WL rapporten*
895 753_09, Flanders Hydraulics Research, Antwerp, Belgium.
- 896 Maximova, T., S. Ides, T. De Mulder, and F. Mostaert (2009b), LTV O & M thema Vei-
897 ligheid - Deelproject 1: Verbetering hydrodynamisch NeVla model ten behoeve van
898 scenario-analyse (in Dutch), *WL rapporten 756_05*, Flanders Hydraulics Research &
899 Deltares, Antwerp, Belgium.
- 900 Maximova, T., S. Ides, T. De Mulder, and F. Mostaert (2009c), Verbetering randvoorwaar-
901 denmodel. Deelrapport 4: Extra aanpassingen Zeeschelde (in Dutch), *WL rapporten*
902 753_09, Flanders Hydraulics Research, Antwerp, Belgium.
- 903 Meersschaet, Y. M. A., W. R. Parker, J. J. Peters, and Y. M. G. Plancke (2004), A dredg-
904 ing and disposal strategy for managing the Western Scheldt's morphology and ecology,
905 in *WODCON XVII: Dredging in a Sensitive Environment*.
- 906 Nicholas, A. P. (2013a), Morphodynamic diversity of the world's largest rivers, *Geology*,
907 41(4), 475–478, doi:10.1130/G34016.1.
- 908 Nicholas, A. P. (2013b), Modelling the continuum of river channel patterns, *Earth Surface*
909 *Processes and Landforms*, 38, 1187–1196, doi:10.1029/2010JF001774.
- 910 Nieuwboer, B. (2012), Numerical modelling of Colorado sandbar growth, Master's thesis,
911 TU Delft.
- 912 Olsen, N. R. (2003), Three-dimensional CFD modelling of self-forming meandering
913 channel, *Journal of Hydraulic Engineering*, 129, 366–372, doi:10.1061/(ASCE)0733-
914 9429(2003)129:5(366).
- 915 Paola, C., P. Heller, and C. Angevine (1992), The large-scale dynamics of grain-size varia-
916 tion in alluvial basins. I: Theory, *Basin Res.*, 4, 73–90.
- 917 Roelvink, J. A. (2006), Coastal morphodynamic evolution techniques, *Coastal Engineer-*
918 *ing*, 53(2–3), 277–287, doi:10.1016/j.coastaleng.2005.10.015.
- 919 Schrijvershof, R., and J. Vroom (2016), Effecten van realistische (extreme) stortstrategieën
920 in de Westerschelde (in Dutch), *Tech. rep.*, Deltares.
- 921 Schuurman, F., M. G. Kleinhans, and W. A. Marra (2013), Physics-based modeling of
922 large braided sand-bed rivers: bar pattern formation, dynamics, and sensitivity, *Journal*
923 *of Geophysical Research – Earth Surface*, 118, 2509–2527, doi:10.1002/2013JF002896.
- 924 Schuurman, F., M. G. Kleinhans, and H. Middelkoop (2016a), Network response to dis-
925 turbances in large sand-bed braided rivers, *Earth Surface Dynamics*, 4, 25–45, doi:
926 10.5194/esurf-4-25-2016.
- 927 Schuurman, F., Y. Shimizu, T. Iwasaki, and M. G. Kleinhans (2016b), Dynamic meander-
928 ing in response to upstream perturbations and floodplain formation, *Geomorphology*,
929 253, 94–109, doi:10.1016/j.geomorph.2015.05.039.
- 930 Silvis, F., and M. B. De Groot (1995), Flow slide in the Netherlands: experience and engi-
931 neering practice, *Canadian Geotechnical Journal*, 32, 1086–1092, doi:10.1139/t95-107.

- 932 Simon, A., and A. J. C. Collinson (2002), Quantifying the mechanical and hydrologic ef-
 933 fects of riparian vegetation on streambank stability, *Earth Surface Processes and Land-*
 934 *forms*, 27(5), 527–546, doi:10.1002/esp.325.
- 935 Torrey, V. H. (1995), Flow slides in Mississippi riverbanks, in *River, Coastal and Shoreline*
 936 *Protection-Erosion Control. Using Riprap and Armourstone*, edited by C. R. Thorne,
 937 S. R. Abt, B. J. Barendt, S. T. Maynard, and K. W. Pilarczyk, pp. 361–377, Wiley,
 938 Chichester.
- 939 Van de Lageweg, W. I., W. M. Van Dijk, A. W. Baar, J. Rutten, and M. G. Kleinhans
 940 (2014), Bank pull or bar push: What drives scroll-bar formation in meandering rivers?,
 941 *Geology*, 42(4), 319–322, doi:10.1130/G35192.1.
- 942 Van de Lageweg, W. I., L. Braat, D. R. Parsons, and M. G. Kleinhans (2018), Controls on
 943 mud distribution and architecture along the fluvial-to-marine transition, *Geology*, doi:
 944 10.1130/G45504.1.
- 945 Van den Berg, J. H., C. J. L. Jeuken, and A. J. F. Van der Spek (1996), Hydraulic pro-
 946 cesses affecting the morphology and evolution of the Western Scheldt estuary, in *Estu-*
 947 *arine Shores*, edited by K. F. Nordstrom and C. T. Roman, pp. 157–184.
- 948 Van den Berg, J. H., A. Van Gelder, and D. R. Mastbergen (2002), The importance of
 949 breaching as a mechanism of subaqueous slope failure in fine sand, *Sedimentology*,
 950 49(1), 81–95, doi:10.1111/j.1525-139X.2006.00168.x-i1.
- 951 Van den Berg, J. H., A. W. Martinius, and R. Houthuys (2017), Breaching-related tur-
 952 bidities in fluvial estuarine channels: Examples from outcrop and core and implications
 953 to reservoir models, *Marine and Petroleum Geology*, 82, 178–205.
- 954 Van den Ham, G. A., M. B. De Groot, and D. R. Mastbergen (2014), A semi-empirical
 955 method to assess flow-slide probability, in *Submarine mass movements and their conse-*
 956 *quences*, vol. 37, edited by S. Krastel, J.-H. Behrmann, D. Volker, M. Stipp, C. Berndt,
 957 R. Urgeles, J. Chaytor, K. Huhn, M. Strasser, and C. B. Harbitz, Advances in Natural
 958 and Technological Hazards Research, Springer International Publishing Switzerland, doi:
 959 10.1007/978-3-319-00972-8.
- 960 Van der Wegen, M., and J. A. Roelvink (2012), Reproduction of estuarine bathymetry by
 961 means of a process-based model: Western Scheldt case study, the Netherlands, *Geomor-*
 962 *phology*, 179, 152–167, doi:10.1016/j.geomorph.2012.08.007.
- 963 Van Dijk, W. M., F. Schuurman, W. I. Van de Lageweg, and M. G. Kleinhans (2014),
 964 Bifurcation instability determines chute cutoff development in meandering gravel-bed
 965 rivers, *Geomorphology*, 213, 277–291, doi:10.1016/j.geomorph.2014.01.018.
- 966 Van Dijk, W. M., D. R. Mastbergen, G. A. Van de Ham, and M. G. Kleinhans (2018a),
 967 Probability and causes of shoal margin collapses in a sandy estuary, *Earth Surface Pro-*
 968 *cesses and Landforms*, doi:10.1002/esp.4395.
- 969 Van Dijk, W. M., M. R. Hiatt, J. J. Van der Werf, and M. G. Kleinhans (2018b), Shoal
 970 margin collapses in Delft3D, GitHub, doi:10.5281/zenodo.1472212.
- 971 van Rijn, L. (1993), *Principles of sediment transport in rivers, estuaries and coastal seas*,
 972 615 pp., Aqua Publications, Oldemarkt.
- 973 Van Rijn, L. C. (2007a), Unified view of sediment transport by currents and waves, i: Ini-
 974 tiation of motion, bed roughness, and bed-load transport, *Journal of Hydraulic Engineer-*
 975 *ing*, 133(6), 649–667.
- 976 Van Rijn, L. C. (2007b), Unified view of sediment transport by currents and waves, ii:
 977 Suspended transport, *Journal of Hydraulic Engineering*, 133(6), 668–689.
- 978 Van Schaick, S. (2015), Morphological development after the July 2014 flow slide on the
 979 tidal flat of Walsoorden in the Western Scheldt, Master’s thesis, Delft University of
 980 Technology.
- 981 Verbeek, H., F. T. G. Tank, and M. D. Groenewoud (1998), Dremfels in de Westerschelde
 982 (in Dutch), *Tech. rep.*, Rijksinstituut voor kust en zee/RIKZ.
- 983 Vroom, J., P. L. M. De Vet, and J. J. Van der Werf (2015), Validatie waterbeweging
 984 Delft3D NeVla model Westerscheldemonding (in Dutch), *Tech. rep.*, Deltares.

- 985 Wang, Z., R. Fokkink, M. de Vries, and A. Langerak (1995), Stability of river bifurcations
986 in 1D morphodynamic models, *Journal of Hydraulic Research*, 33(6), 739–750.
- 987 Wang, Z. B. (2015), Sustainability of the multi-channel system in the Westerschelde under
988 influence of dredging and disposal, in *Scheldt Estuary, physics and integrated manage-*
989 *ment*, pp. 65–70, IAHR.
- 990 Wang, Z. B., A. Langerak, and R. J. Fokkink (1999), Simulation of long-term morpholog-
991 ical development in the Western Scheldt, in *River, Coastal and Estuarine Morphodynam-*
992 *ics*, pp. 367–376.
- 993 Whipple, K. X., and G. E. Tucker (1999), Dynamics of the stream-power river inci-
994 sion model: Implications for height limits of mountain range, landscape response
995 timescales, and research needs, *Journal of Geophysical Research - Solid Earth*, 104(B2),
996 17,661–17,674, doi:10.1029/1999JB900120.
- 997 Wilderom, M. H. (1961), Tussen afsluitdammen en deltadijken (in dutch), *Tech. rep.*, Rijk-
998 swaterstaat, Vlissingen, The Netherlands.
- 999 Wilderom, M. H. (1972), Plaatvallen (in dutch), *OTAR*, 57(7), 288–305.
- 1000 Wilderom, M. H. (1979), Resultaten van het vooronderzoek langs de Zeeuwse
1001 stromen (in Dutch), *Tech. rep.*, Rijkswaterstaat, nota 75.2.
- 1002 Winterwerp, J. C., M. C. J. L. Jeuken, M. J. F. Stive, and H. J. De Vriend (2000), Lange
1003 termijnvisie Westerschelde - Cluster Morfologie (in Dutch), *Tech. rep.*, WL Delft Hy-
1004 draulics.
- 1005 Xu, J. (1997), Evolution of mid-channel bars in a braided river and complex re-
1006 sponse to reservoir construction: an example from the middle Hanjiang River,
1007 China, *Earth Surface Processes and Landforms*, 22, doi:10.1002/(SICI)1096-
1008 9837(199710)22:10<953::AIDESP789>3.0.CO;2-S,.

1009

Table 1. Model scenarios

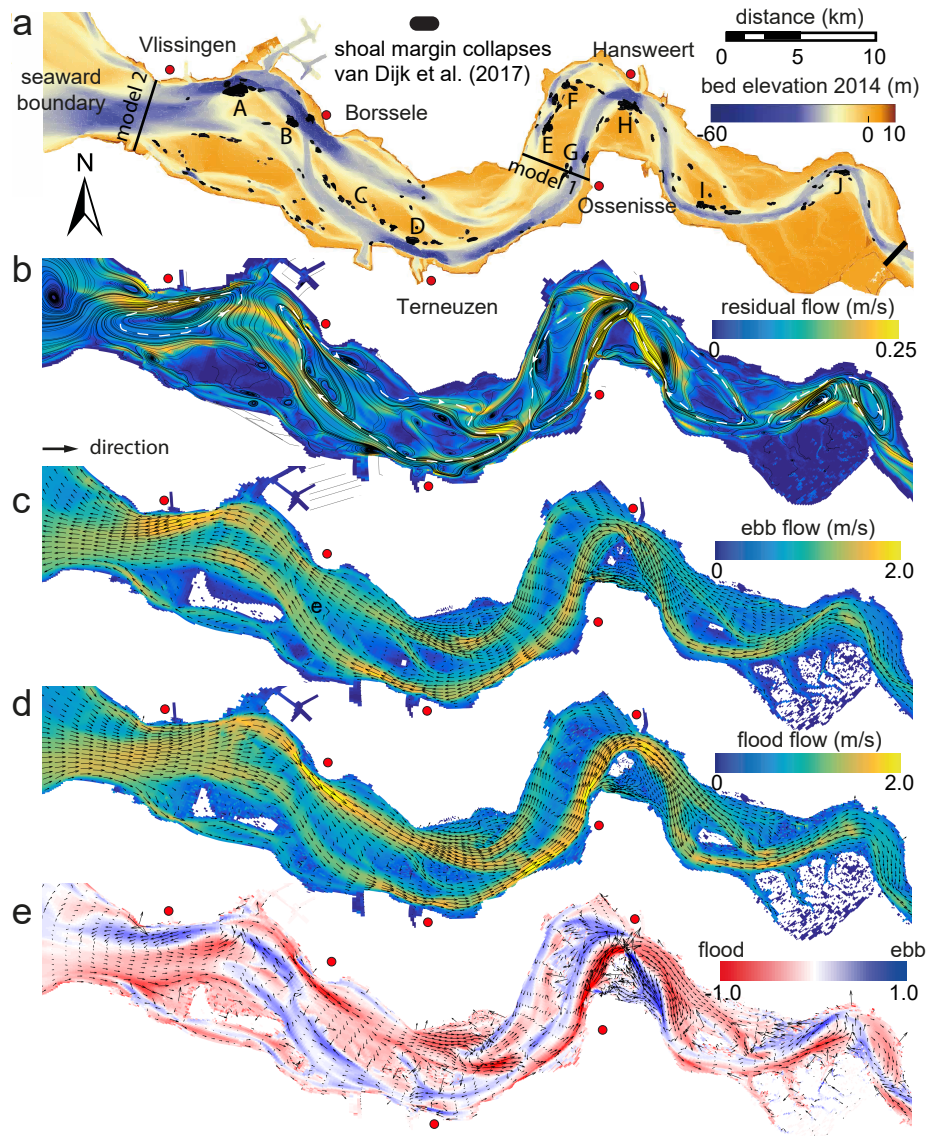
Scenario	Model	Test	duration	comments
1	1	2014 collapse	1 year	see <i>Van Schaick</i> [2015]
2	2	initial 10 collapses	40 years	see locations Figure 1a
3	2	yearly collapses	40 years	rule based on <i>Van Dijk et al.</i> [2018a]
Sensitivity scenarios				
collapse size	1	100,000 m ³ vs. 1,000,000 m ³	1 year	see Supplementary
grain size	1	100 μ m vs. 200 μ m vs. 300 μ m	1 year	see Supplementary
α_{bn}	1	1.5 vs. 30	1 year	see Supplementary

1010

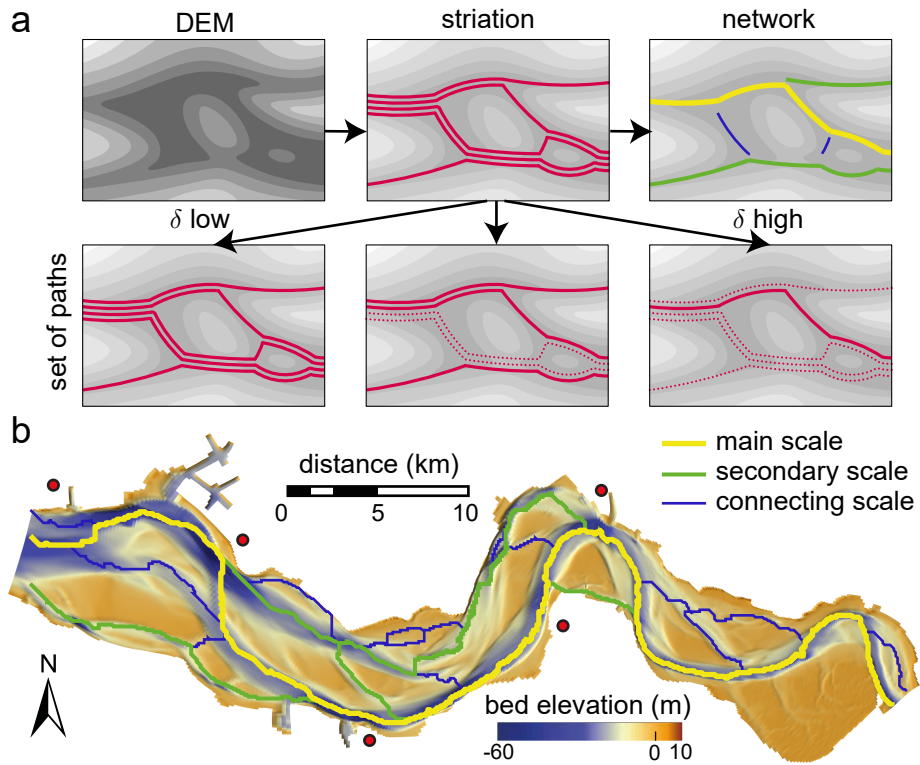
Table 2. Statistics of the mean μ and standard deviation σ of the depth for the various runs for all network scales.

1011

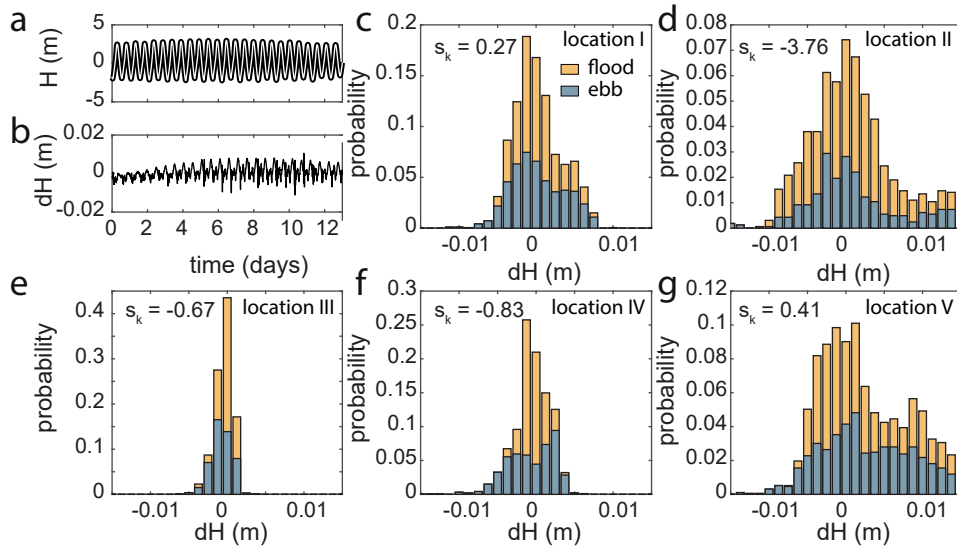
Scale	μ (m)				σ (m)			
	initial	control	2	3	initial	control	2	3
main	-23.91	-26.16	-25.79	-25.73	8.16	10.95	11.13	11.02
secondary	-15.65	-17.41	-17.88	-19.15	7.19	10.87	10.11	11.93
connecting	-10.60	-12.23	-10.62	-12.35	6.60	8.00	5.95	7.09



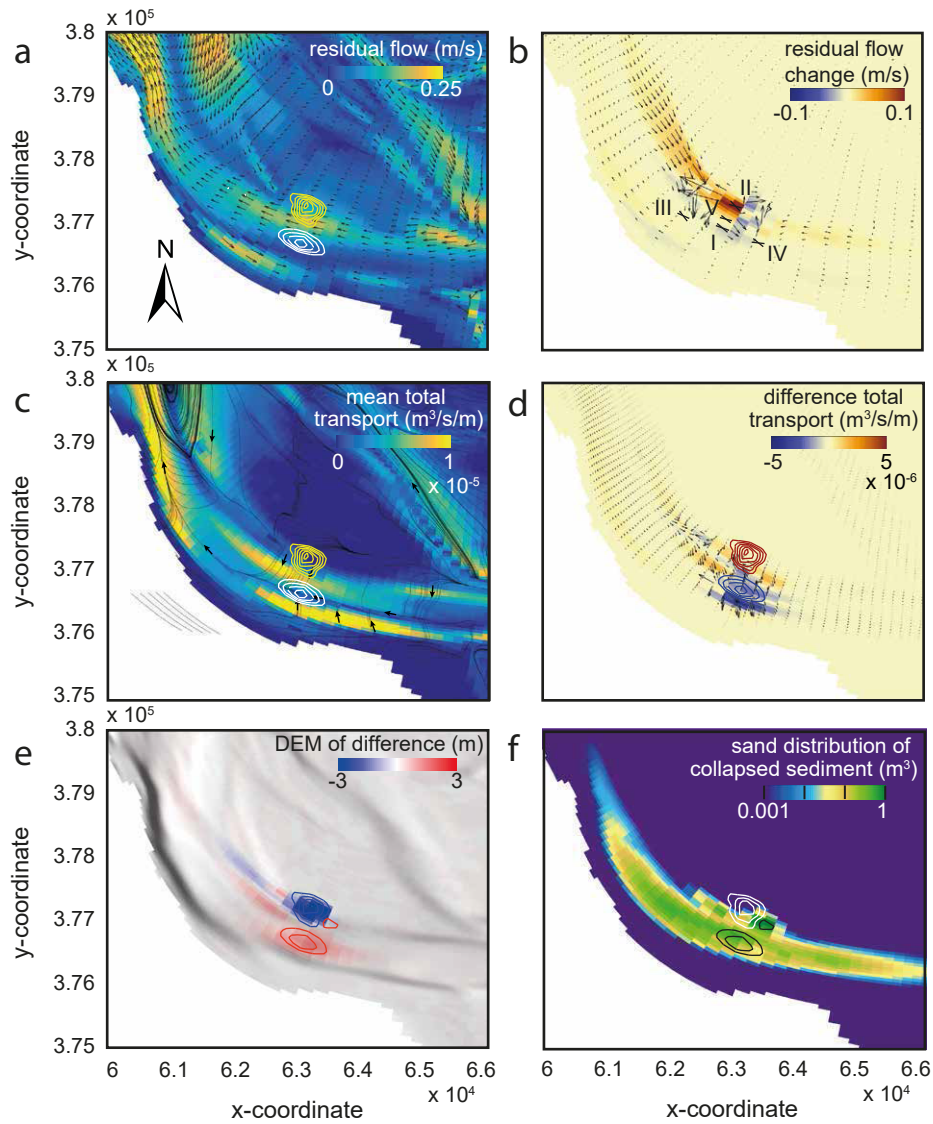
1012 **Figure 1.** Overview of hydromorphodynamics in the Western Scheldt Estuary. a) Shoal margin collapse
 1013 locations plotted on a digital elevation model of January 2014 [Van Dijk et al., 2018a]. Seaward boundaries
 1014 are indicated for the two morphological model schematizations in this study. A-J indicate locations suscep-
 1015 tible to shoal margin collapses that are applied in the model scenario with ten initial collapses, and refer to
 1016 the locations for Figures 5 and 6. b) Streamlines of the tidally-averaged flow of the original NeVla-Delft3D
 1017 flow model showing circulation cells that correspond largely to the macro cells indicated in white defined
 1018 by Winterwerp et al. [2000] and Bolle et al. [2010]. c) Maximum flow velocity in the ebb-direction from the
 1019 NeVla-Delft3D model. d) Maximum flow velocity in the flood-direction from the NeVla-Delft3D model. e)
 1020 Difference (in m/s) between the maximum ebb and maximum flood velocity showing flood dominance in the
 1021 main channels.



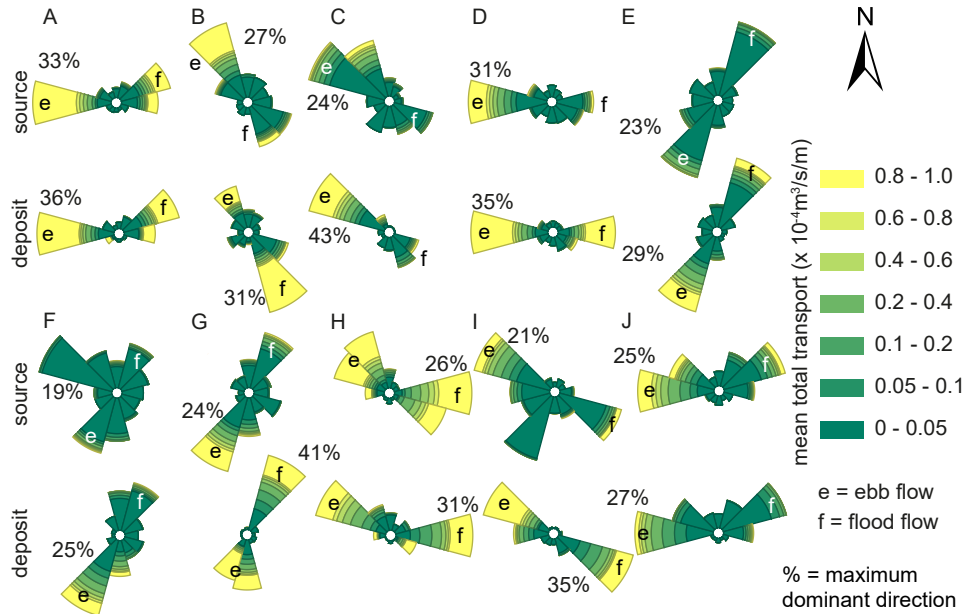
1022 **Figure 2.** Illustration of the network extraction approach. a) First, from the DEM, the striation is computed
 1023 (top). Then, different paths are found (represented by three sand function values, δ , which form the final net-
 1024 work including the main, secondary and connecting scale. c) Example network for the initial bathymetry of
 1025 the Western Scheldt.



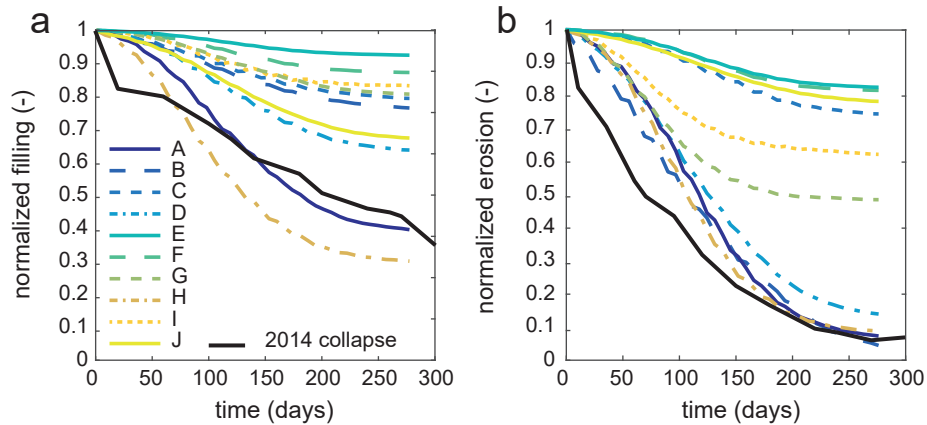
1026 **Figure 3.** Changes in the water elevation relative to the control run at the 5 surrounding grid cells of the
 1027 shoal margin collapse of 2014 (locations in Figure 4b). a) Water level at location of the collapsed sediment
 1028 deposit (location I) for a simulation without (thick black line) and with the 2014 shoal margin collapse (thin
 1029 white line on top). b) Difference in water surface elevation at the deposited collapsed sediment is within 1 cm.
 1030 Positive values indicate water level rise following the collapse. c) Distribution of water level change shows a
 1031 slight increase in the water level. Here, s_k indicates if the distribution is skewed to the left (negative) or right
 1032 (positive) from the mean of the distribution, where the mean is 0 m for all distributions. The two different col-
 1033 ors show differences between ebb and flood conditions but no systematic lower or higher water levels. d) The
 1034 water level generally decreases. e) Seaward there is a slight difference in the water level, whereas f) landward
 1035 there is more difference as in generally the water level lowers. g) Water level increases on the shoal margin.



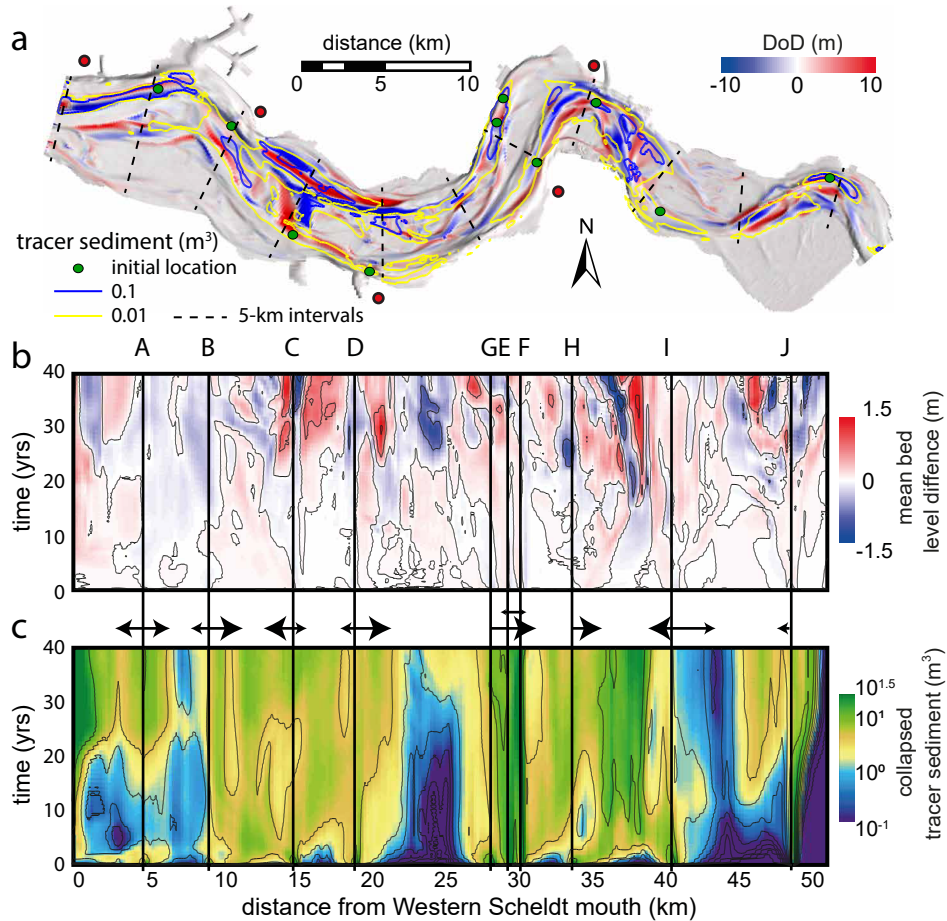
1036 **Figure 4.** Hydromorphodynamics at a single shoal margin collapse after 1 year compared with a run with-
 1037 out the collapse. a) The tidally-averaged flow modeled for the control run shows ebb-dominated flow along
 1038 the shoal margin collapse of 2014 (yellow), while at the deposit (white) it is around zero. The contour lines
 1039 were plotted at 1 m elevation intervals. b) Tidally-averaged flow increases along the shoal margin seaward
 1040 of the collapse and slows down at the collapse. Crosses numbered I-V are the locations for water elevation
 1041 shown in Figure 3. c) The mean total transport is ebb-dominated at the shoal margin (note vectors), but, as
 1042 $\alpha_{bn} = 30$, as a large transverse component into the channel along the Tidal flat of Walsoorden. d) The to-
 1043 tal transport reduces around the shoal margin collapse. e) The deposited sediment is spread only directly
 1044 landward and seaward of the collapse, whereas the eroded collapse location remains unfilled. f) Sediment is
 1045 spread dominantly in seaward direction in the channel along the vectors of the mean total sediment transport
 1046 (see Figure 4c).



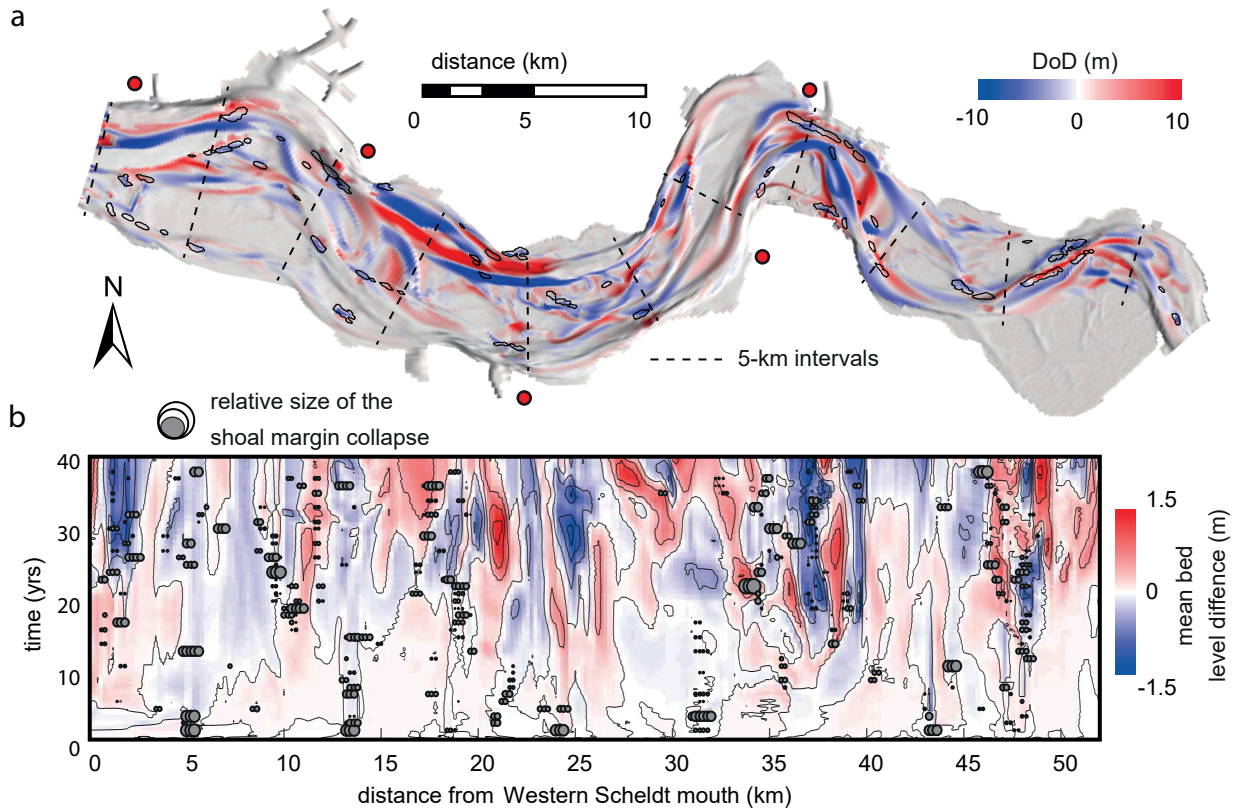
1047 **Figure 5.** Total sediment transport magnitude and direction for various collapse locations (see locations in
 1048 Figure 1a) show dominantly ebb and flood flow-related directions for the first year after the collapse. At the
 1049 shoal margin collapse locations (top rose diagram) less transport is calculated and at some locations a third
 1050 dominant direction is observed because of the transverse bed slope effect (see F and I). Sediment transport is
 1051 generally higher for the deposited sediment (bottom rose diagram). The percentage indicates the maximum
 1052 duration of the dominant direction.



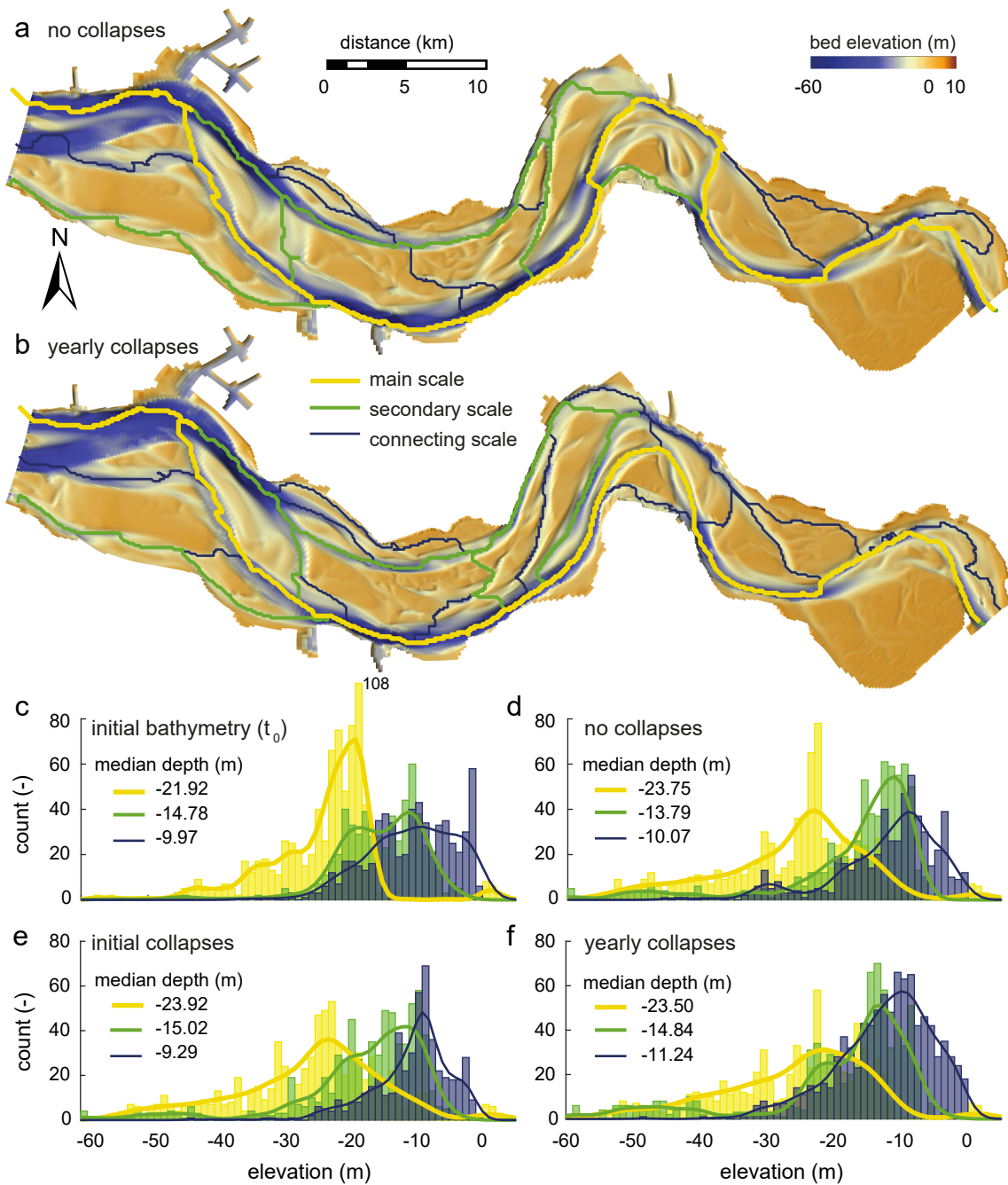
1053 **Figure 6.** Development of shoal margin collapse scar and deposit volumes normalized by its initial volume
 1054 at various locations for the Delft3D simulation in the first year (see locations in Figure 1a). The observed
 1055 shoal margin collapse of 2014, close to modelled location I, is shown for comparison [see *Van Schaick, 2015*].
 1056 a) Filling of the scar varies with location, but is never completed within a single morphological year. b) De-
 1057 posit removal is faster than scar filling. In particular shoal margin collapses in secondary channels develop
 1058 slowly, e.g. tidal flats of Brouwerplaat (E) and Molenplaat (F), and the less dynamic landward part of the
 1059 estuary, Verdronken Land van Saeftinghe (J). Wiggles indicate effects of neap-spring tidal cycles.



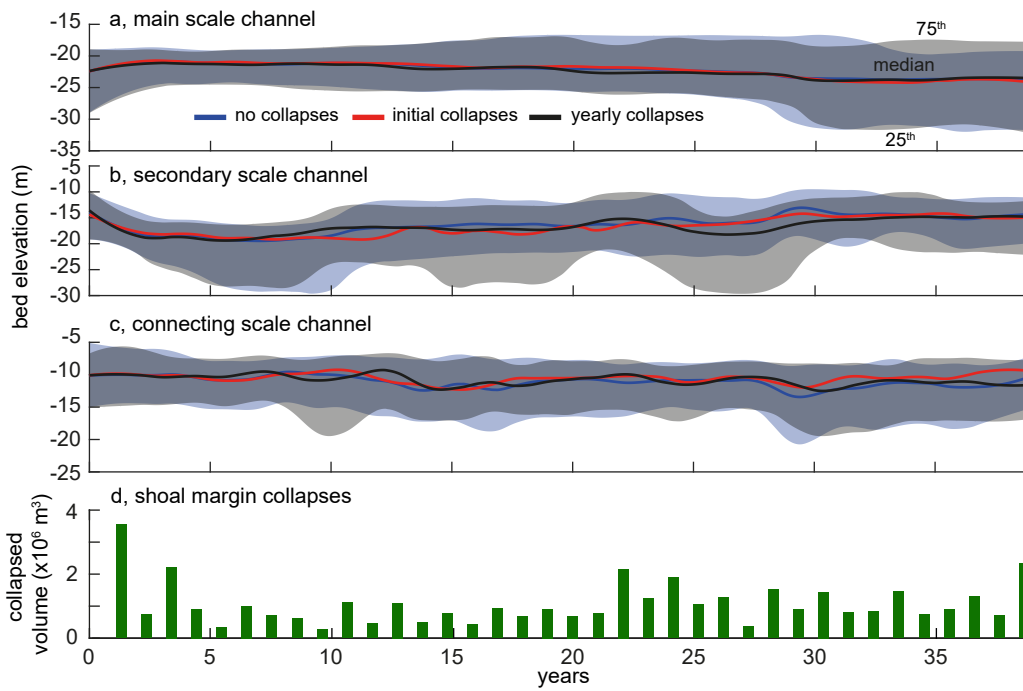
1060 **Figure 7.** Effect of multiple initial collapses in the Western Scheldt. a) Elevation difference after 40 years
 1061 between a simulation with and without 10 shoal margin collapses shows that for several locations the per-
 1062 turbation has migrated landward as well as seaward, whereas other collapses hardly migrated over 40 years,
 1063 e.g., locations E and F (see Figure 1a). The colored contour lines show the spatial distribution of the col-
 1064 lapsed material. b) Width-averaged bed elevation difference between the run with and without initial collapses
 1065 shows some migration of the perturbations but mainly shows cumulative excitation effects after two decades.
 1066 c) Spatiotemporal distribution of the collapsed sediment, showing spreading in both seaward and landward
 1067 directions.



1068 **Figure 8.** a) Bed elevation difference between a control run and a run with yearly shoal margin collapses
 1069 (indicated by the contour lines) shows that the entire system is modified, especially at junctions forming
 1070 ebb-flood channels (landward of location B and at location H). b) Width-averaged bed elevation difference
 1071 between both runs shows location of incision and deposition that migrates, excites or dampens depending on
 1072 the location of the collapse.



1073 **Figure 9.** Networks in (a) the control run without collapses and (b) the scenario with yearly collapses,
 1074 showing that spatial channel shifts and changes in scale of channels after 40 years morphological develop-
 1075 ment. c-f) Depth distributions of the channel networks shows a deep initial main channel (c), which becomes
 1076 shallower when modeled (d). The depth distribution for the run with initial collapses develops towards the
 1077 control run (e), whereas continuous yearly collapses lead to further shallowing of main channel in the estuary
 1078 (f).



1079 **Figure 10.** Depth over time for the three model runs illustrating an increasing variation in depth for the
 1080 various network scales. a) Median depth for the main channel network over time shows minor differences with
 1081 the control run. b) Secondary channel network deviates after 10 years for the run with yearly collapses. c)
 1082 Connecting channel network shows faster response time to collapses. Shading indicates quartiles. Consider-
 1083 able deviations are observed for the yearly collapses at 9, 18 and 30 years and for the initial collapses at 13, 27
 1084 and 36 years. d) Time and volume of shoal margin collapses for the scenario with yearly collapses.